



저작자표시-비영리-변경금지 2.0 대한민국

이용자는 아래의 조건을 따르는 경우에 한하여 자유롭게

- 이 저작물을 복제, 배포, 전송, 전시, 공연 및 방송할 수 있습니다.

다음과 같은 조건을 따라야 합니다:



저작자표시. 귀하는 원저작자를 표시하여야 합니다.



비영리. 귀하는 이 저작물을 영리 목적으로 이용할 수 없습니다.



변경금지. 귀하는 이 저작물을 개작, 변형 또는 가공할 수 없습니다.

- 귀하는, 이 저작물의 재이용이나 배포의 경우, 이 저작물에 적용된 이용허락조건을 명확하게 나타내어야 합니다.
- 저작권자로부터 별도의 허가를 받으면 이러한 조건들은 적용되지 않습니다.

저작권법에 따른 이용자의 권리는 위의 내용에 의하여 영향을 받지 않습니다.

이것은 [이용허락규약\(Legal Code\)](#)을 이해하기 쉽게 요약한 것입니다.

[Disclaimer](#)

Thesis for the Degree of Doctor of Philosophy (Ph.D.)

Voxel-based dosimetry of iron oxide
nanoparticles based ^{177}Lu -labeled
folate conjugates targeted SPECT/CT
imaging of mice

August 2018

Department of Medicine
Nuclear Medicine

The Graduate School
College of Medicine
Seoul National University

Arun Gupta

의학박사 학위논문

Voxel-based dosimetry of iron oxide
nanoparticles based ^{177}Lu -labeled
folate conjugates targeted SPECT/CT
imaging of mice

SPECT/CT를 이용한 생쥐에서 ^{177}Lu 표지 산화철
나노입자 기반 엽산 복합체의 복셀 기반 피폭선량
연구

2018 년 08 월

서울 대학교 대학원
의학과 핵의학 전공

Arun Gupta

Voxel-based dosimetry of iron oxide nanoparticles based ^{177}Lu -labeled folate conjugates targeted SPECT/CT imaging of mice

by
Arun Gupta

A Ph.D. thesis submitted to the Department of Nuclear Medicine in partial fulfillment of the requirements for the Degree of Doctor of Philosophy in Medical Science at Graduate School of College of Medicine, Seoul National University

Thesis committee approved the Ph.D. Thesis
written by
Arun Gupta

August 2018

Chair _____(Seal)
Vice Chair _____(Seal)
Examiner _____(Seal)
Examiner _____(Seal)
Examiner _____(Seal)

SPECT/CT를 이용한 생쥐에서 ^{177}Lu 표지 산화철 나노입자 기반 엽산 복합체의 복셀 기반 피폭선량 연구

지도교수 이 동 수

이 논문을 의학박사 학위논문으로 제출함

2018 년 08 월

서울 대학교 대학원
의학과 핵의학 전공

Arun Gupta

Arun Gupta의 의학박사 학위논문으로 이준함

2018 년 08 월

위원장 _____ (인)
부위원장 _____ (인)
위 원 _____ (인)
위 원 _____ (인)
위 원 _____ (인)

Abstract

Voxel-based dosimetry of iron oxide nanoparticles based ^{177}Lu -labeled folate conjugates targeted SPECT/CT imaging of mice

Arun Gupta

Department of Nuclear Medicine

The Graduate School

Seoul National University

Peptide-receptor radionuclide therapy (PRRT) has gained increasing importance for the treatment of various cancers including lymphoma, glioblastoma, neuroendocrine tumors and prostate cancer. The effectiveness of targeted radionuclide therapy (TRT) depends primarily on the absorbed dose rate and the total absorbed dose delivered to the tumor and to normal tissues. Hence, the absorbed dose must be determined as accurately as possible to obtain appropriate absorbed dose response-effect relationships. Due to the various limitations associated with organ-based dosimetry performed by MIRD schema, the voxel-based dosimetry has become essential for the assessment of more accurate absorbed dose.

The folate receptor (FR) has been identified as a target associated with varieties of tumors including ovarian and cervical carcinoma. Therefore, several folic acid conjugates using diagnostic and therapeutic radionuclides have been developed for targeted imaging and therapy. However, the therapeutic concept with radiolabeled folate conjugates has not been applied yet for clinical application due to higher renal absorbed dose caused by increased uptake in kidneys. To overcome these challenges, we prepared iron oxide nanoparticle

(IONPs) based radiolabeled folate conjugate (^{177}Lu -IONPs-Folate) and performed voxel-based dosimetry using SPECT/CT imaging of normal mice. In this thesis, we first performed voxel-based dosimetry in normal mice from whole-body ^{18}F -fluorodeoxyglucose (^{18}F -FDG) PET/CT imaging to evaluate the feasibility and reliability of image-based preclinical dosimetry using GATE MC toolkit. Secondly, we evaluated system performance and quantitative accuracy of NanoSPECT/CT scanner for ^{177}Lu radioisotope using point source and uniform phantom studies. Finally, we estimated the absorbed doses at voxel-level using GATE MC from the SPECT/CT images of normal mice performed with ^{177}Lu -Folate, ^{177}Lu -IONPs and ^{177}Lu -IONPs-Folate. We also calculated organ-based absorbed dose in the given organs due to all three radiotracers using MIRD schema.

MC simulation considers the true activity distribution and tissue heterogeneity during whole-body absorbed dose estimation at voxel-level. Therefore, the voxel-based absorbed dose estimated in the organs of mice from ^{18}F -FDG PET would be more accurate. The results obtained from measured performance parameters were convincing to conduct preclinical SPECT/CT imaging. We found that the absorbed dose to the kidneys was significantly decreased when Iron-oxide nanoparticle based ^{177}Lu -labeled folate conjugate (^{177}Lu -IONPs-Folate) was used compared to ^{177}Lu -Folate.

In conclusion, the absorbed dose values in the organs obtained at voxel-level using individualized activity and media distributions would be more accurate. This method can be used for personalized dosimetry in TRT to estimate maximum tolerated activity for therapy planning.

Keywords: SPECT/CT, Voxel-based dosimetry, GATE Monte Carlo, ^{177}Lu , Folate Receptors, IONPs
Student Number: 2015-30884

Contents

Abstract	i
Contents	iii
List of Figures	vi
List of Tables.....	ix
General Introduction	1
Chapter 1. Feasibility and reliability of GATE MC for Preclinical voxel-based dosimetry	5
1.1. Background	5
1.2. Materials and Methods	7
1.2.1. Animal reparation	7
1.2.2. PET/CT acquisition	7
1.2.3. Organ mass estimation and image-based biodistribution	7
1.2.4. GATE MC simulation	9
1.2.5. Voxel-based dosimetry method	10
1.2.6. Organ-based dosimetry method	11
1.3. Results.....	12
1.3.1 PET Image-based biodistribution	12
1.3.2 Energy deposition and dose rate	12
1.3.3 Voxel-based absorbed dose	14
1.3.4 Organ-based absorbed dose	14
1.3.5 Voxel-based vs. organ-based absorbed dose	15
1.4. Discussion	17

Chapter 2. Performance Evaluation of NanoSPECT/CT	
Scanner for ^{177}Lu imaging	19
2.1. Background	19
2.2. Materials and Methods	21
2.2.1. NanoSPECT/CT system	21
2.2.2. Point source and uniform phantom acquisition	21
2.2.3. Adding uniform background to point source data	23
2.2.4. Image reconstruction	23
2.2.5. System performance evaluation	24
2.3. Results	29
2.3.1. Recovery coefficient and uniformity	29
2.3.2. Spatial resolution	31
2.3.3. System sensitivity	32
2.3.4. Calibration factor	34
2.4. Discussion.....	35
Chapter 3. Voxel-based dosimetry of ^{177}Lu-labeled	
folate conjugates targeted SPECT/CT imaging of mice.....	36
3.1. Background.....	36
3.2. Materials and Methods.....	38
3.2.1. Synthesis of ^{177}Lu -labeled folate conjugates	38
3.2.2. Animal preparation	40
3.2.3. ^{177}Lu -SPECT/CT Imaging	40
3.2.4. Image reconstruction	41
3.2.5. SPECT image-based biodistribution of	
radiotracers	41
3.2.6. GATE MC simulation set up	43

3.2.7. Voxel-based dosimetry method	43
3.2.8. Organ-based dosimetry method	44
3.3. Results	45
3.3.1. SPECT image-based biodistribution	45
3.3.2. Energy deposition and dose rate	46
3.3.3. Voxel-based absorbed dose	48
3.3.4. Organ-based absorbed dose	51
3.3.5. Discussion	53
General Discussion and Conclusion	56
References	59
Abstract in Korean	66

List of Figures

Figure 1.1. VOIs drawn on brain, heart wall and bladder wall on CT images (a) and 90 minutes time integrated PET image (b). Figure shows the VOIs are superimposed on selected PET frames (c-h) at different time post injection. Coronal (left) and sagittal (right) views of CT and PET images are shown respectively in the figure.4

Figure 1.2. GATE MC simulation study for voxel-based absorbed dose estimation. 6

Figure 1.3. Percentage injected dose (%ID, mean \pm SD) versus time of the eight organs (corrected for radiation decay). SD, standard deviation.8

Figure 1.4. PET/CT fused image (a), E_{dep} map (b) and the E_{dep} map overlaid on CT image (c). The E_{dep} map shows the energy deposited was higher for bladder wall, heart wall, kidneys and brain compared to other organs. Coronal (left) and sagittal (right) views of the images are shown respectively in the figure.9

Figure 1.5. Dose-rate (mean \pm SD) versus time graph for the eight organs (uncorrected for radiation decay). SD, standard deviation.9

Figure 1.6. Percentage difference (mean \pm SD) between voxel-based absorbed dose estimated by GATE MC simulation and organ-based absorbed dose estimated by MIRD schema. 12

Figure 1.7. Comparison of voxel-based and organ-based absorbed dose calculated from ^{18}F -FDG in selected organs of mice between this study and those reported by Xie et al. and Taschereau and Chatziioannou.12

Figure 2.1. SPECT point source projections were acquired at center of axial and transaxial FOV and repeated at every 2 mm from the center. Axial FOV: 14 mm; Transaxial FOV: 30 mm. 18

Figure 2.2. Reconstructed point source image of ^{177}Lu positioned at center of transaxial FOV. a) without background; b) after adding uniform background; c) VOIs drawn over background added point image; d) VOIs drawn over background regions. 21

Figure 2.3. Reconstructed point source image of $^{99\text{m}}\text{Tc}$ positioned at center of transaxial FOV. a) without background; b) after adding uniform background; c) VOIs drawn over background added point image; d) VOIs drawn over background regions. 22

Figure 2.4. Reconstructed SPECT images of uniform phantoms containing ^{177}Lu (a) and $^{99\text{m}}\text{Tc}$ (b). VOIs were drawn over the central portion of the phantom images. 23

Figure 2.5. Scattered plot between recovery coefficients (RCs) and %SDs measured from reconstructed point source image with increasing number of iterations (3 to 30) for ^{177}Lu and $^{99\text{m}}\text{Tc}$. Iteration numbers are denoted by shapes in the figure where first shape indicates three iterations; second shape indicates six and so on up to thirty iterations. 26

Figure 2.6. The relationship between %SDs of uniform phantom images and the number of iterations (3 to 30) for ^{177}Lu and $^{99\text{m}}\text{Tc}$ 26

Figure 2.7. FWHM measured from ^{177}Lu (a) and $^{99\text{m}}\text{Tc}$ (b) point source images at center and other positions with and without adding uniform background in axial, radial and tangential directions. BKG, Background. 28

Figure 2.8. System sensitivities measured from ^{177}Lu and $^{99\text{m}}\text{Tc}$ point source projection data acquired at different positions in axial (a) and transaxial (b) FOVs. 29

Figure 3.1. CT images acquired at different time points during SPECT/CT acquisitions (upper row) of mice. VOIs were drawn over the organs (brain, heart, lungs, liver and kidneys on the CT images (lower row). 38

Figure 3.2. SPECT/CT MIP images of a mouse acquired at different time points after injection of ^{177}Lu -Folate (a), ^{177}Lu -IONPs (b) and ^{177}Lu -IONPs-Folate (c). For ^{177}Lu -IONPs-Folate, 72-hour image could not be acquired due to technical problem in the scanner.42

Figure 3.3. Percentage injected dose (%ID, mean) versus time graphs (TACs) of organs (corrected for radiation decay) obtained for ^{177}Lu -Folate (a), ^{177}Lu -IONPs (b) and ^{177}Lu -IONPs-Folate (c). 43

Figure 3.4. Edep maps (obtained from GATE simulation of SPECT/CT imaging data) overlaid on CT (MIP images) images of mouse. ^{177}Lu -Folate (a), ^{177}Lu -IONPs (b) and ^{177}Lu -IONPs-Folate (c).....48.

Figure 3.5. Dose-rate (mean) versus time graphs of organs (uncorrected for radiation decay) plotted for ^{177}Lu -Folate (a), ^{177}Lu -IONPs (b) and ^{177}Lu -IONPs-Folate (c). 44

Figure 3.6. Comparison of voxel-based absorbed (mean \pm SD) in major organs from ^{177}Lu -Folate, ^{177}Lu -IONPs and ^{177}Lu -IONPs-Folate. ... 46

Figure 3.7. Difference in voxel-based absorbed dose (mean \pm SD) in organs between ^{177}Lu -IONPs-Folate and ^{177}Lu -Folate. The absorbed dose was significantly reduced with ^{177}Lu -IONPs-Folate.46

Figure 3.8. Comparison of voxel-based absorbed dose (mean \pm SD) estimated by GATE MC with organ-based self-absorbed dose (mean \pm SD) calculated with MIRD schema for ^{177}Lu -Folate, ^{177}Lu -IONPs and ^{177}Lu -IONPs-Folate. VB, voxel-based; OB, organ-based. 47

Figure 3.9. Difference between voxel-based absorbed dose (mean \pm SD) estimated by GATE MC and organ-based self-absorbed dose (mean \pm SD) calculated with MIRD schema for ^{177}Lu -Folate, ^{177}Lu -IONPs and ^{177}Lu -IONPs-Folate. Maximum difference was observed with ^{177}Lu -IONPs-Folate for liver.48

List of Tables

Table 1.1. Voxel-based absorbed dose estimated in major organs (mean \pm SD) from ^{18}F -FDG using GATE MC.	10
Table 1.2. Organ-based absorbed dose (self, cross and total) estimated in major organs (mean \pm SD) from ^{18}F -FDG using MIRD schema normalized per MBq administered activity.	11
Table 3.1. Voxel-based absorbed dose (mean \pm SD) in major organs from ^{177}Lu -Folate, ^{177}Lu -IONPs and ^{177}Lu -IONPs-Folate.	45
Table 3.2. Organ-based absorbed (mean \pm SD) in major organs estimated by MIRD schema from ^{177}Lu -Folate, ^{177}Lu -IONPs and ^{177}Lu -IONPs-Folate.	47

General Introduction

Targeted radionuclide therapy especially peptide receptor radionuclide therapy (PRRT) has gained increasing importance for the treatment of various cancers types including lymphoma, glioblastoma, neuroendocrine tumors and prostate cancer (1-6). For the successful PRRT, selective concentration and prolonged retention of the radiopharmaceutical within the tumor is required (7). Various new radiopharmaceuticals conjugated with peptides are being developed to target the specific receptor present in particular cancer type. Peptide analogs such as RGD, GRP, octreotide, folate etc. are conjugated with suitable radionuclides to target the receptors overexpressed on various cancers such as glioma, ovarian cancer, neuroendocrine tumor, cervical cancer etc. (8, 9). Folate receptors (FRs) are membrane bound glycoproteins, which are highly expressed in many human malignancies such as ovarian, cervical, renal, lung and breast carcinomas (10). However, there are very limited expression of these receptors in normal organs and tissues.

Radionuclide imaging techniques such as single photon emission computed tomography (SPECT) and positron emission tomography (PET) are widely used for preclinical radiopharmaceutical development (11, 12). PET imaging has been considered as more accurate for quantitative studies due to its higher sensitivity (13). However, number of physical parameters affect the SPECT image quantification that include photon attenuation, scattering, and partial volume errors (14). Hence, the integrated SPECT/CT image-based methods are emphasized, because the CT-derived anatomic information may address the multiple technical factors that influence

SPECT image quantification (15).

Many radioisotopes can be used as radiation sources however; very few have been developed and applied in preclinical in vivo imaging and therapy such as ^{111}In , ^{68}Ga , ^{64}Cu , ^{90}Y , ^{188}Re and ^{177}Lu . Folic acid conjugated with theranostic radionuclide especially ^{177}Lu has been used as valuable tool to implement novel and effective anticancer therapies (16). Despite the excellent tumor targeting ability of such radiotracers, a substantial fraction of radioactivity is always found in the kidneys due to the presence of FRs in the proximal tubule cells (17-19). Hence, there is always a risk of radiation-induced nephropathy to the radiosensitive kidneys by particle emitting radioisotopes. Folate-based radiopharmaceuticals with prolonged blood circulation time may be required that could improve the dissatisfying situation.

Recently due to the advancement in nanotechnology, novel nanoparticles such as, gold nanoparticles (AuNPs), iron-oxide nanoparticles (IONPs), quantum dots, dendrimers, micelles etc. have been developed for in vivo molecular imaging and TRT (20-22). Once the nanoparticles are conjugated to therapeutic radioisotopes for tumor targeting, they are trapped in the tumor by enhanced permeability and retention (EPR) effect and the further active targeting can be achieved by binding the appropriate ligands to the surface of the nanoparticles (23). IONPs have a large surface area that provide a large number of functional groups for cross-linking to tumor-targeting ligands such as monoclonal antibodies or peptides for diagnostic imaging or targeted therapy (21).

During TRT, absorbed dose must be determined as accurately as possible to obtain appropriate preclinical absorbed dose response-effect relationships. (24, 25). Absorbed doses in small animals have

been calculated using Medical Internal Radiation Dose (MIRD) formalism that uses S-values (mean absorbed dose in a target organ per radioactivity decay in a source organ) (26, 27). However, organ-based MIRD approach does not incorporate patient- or animal-specific activity distributions and geometries because it assumes homogeneous activity distributions in organs and a generalized geometry (26). Many researchers have addressed the limitations associated with organ-based MIRD method and hence voxel-based dosimetry was implemented to estimate more accurate absorbed dose in organs (28-30). A number of Monte Carlo (MC) radiation transport codes such as MCNP, EGSnrc, Geant4 etc. are available and widely used for voxel-based dosimetry (31).

The Geant4 Application for Emission Tomography (GATE) MC simulation platform based on the Geant4 toolkit, has been gaining its importance for voxel-based dosimetry application (32-34). To the best of our knowledge, very few preclinical dosimetry studies have been performed using GATE MC (25, 35-37). All these studies have used the MOBY phantom developed by Segars et al. (37) which are based on non-uniform rational B spline (NURBS) mathematical models.

Most recently, Theodora et al. (25) calculate the S-values of radioisotopes including ^{177}Lu with whole-body heterogeneous activity distributions as source organ using GATE MC simulation and MOBY phantom. Since the small variations in mice anatomy can result in significant differences in absorbed dose calculations, they concluded that there could not be a specific mouse model with standardized organs and anatomy to implement dosimetry for murine studies. In this thesis, we first performed voxel-based dosimetry of ^{18}F -fluorodeoxyglucose (^{18}F -FDG) in normal mice from whole-body PET/CT imaging to evaluate the feasibility and reliability of image-

based preclinical dosimetry using GATE MC toolkit. Secondly, we performed system performance evaluation of NanoSPECT/CT scanner (Bioscan Inc.,) for ^{177}Lu radioisotope using point source and uniform phantom studies to determine the quantitative accuracy. Finally, we estimated the absorbed doses at voxel-level using GATE MC from the SPECT/CT images of normal mice performed with ^{177}Lu -Folate, ^{177}Lu -IONPs and ^{177}Lu -IONPs-Folate. We also calculated organ-based absorbed dose in the given organs due to all three radiotracers using MIRD schema.

Chapter 1. Feasibility and reliability of GATE MC for preclinical voxel-based dosimetry

1.1. Background

Internal dosimetry has been performed using the standard methods recommended by Medical Internal Radiation Dose (MIRD) committee of the Society of Nuclear Medicine and Molecular Imaging (SNMMI) (26, 27). MIRD schema uses S-values, which represent the mean absorbed dose in a target organ per radioactivity decay in a source organ. However, this approach does not incorporate patient- or animal-specific activity distributions and geometries since it assumes homogeneous activity distributions in organs and a generalized geometry (26). The limitations associated with organ-based MIRD method have been addressed by several researchers (28–30) and various steps have been taken to improve dosimetry results by moving from organ-based dosimetry to voxel-based dosimetry.

Various MC codes (MCNP, EGSnrc, Geant4 etc.) are available and widely used for voxel-level dosimetry, which can consider the non-uniform activity distributions in organs (31). Recently, the GATE MC simulation platform based on the Geant4 toolkit, has gained its importance in voxel-based dosimetry (32, 33). Although the GATE has been widely validated, there are very limited studies reporting its application and reliability in the context of preclinical dosimetry (25, 35–37). All these studies were performed on MOBY phantom developed by Segars *et al.* (38).

Since the small variations in mice anatomy can produce large

differences in dose calculations, there could not be a fixed mouse model with standardized organs and anatomy to implement dosimetry for murine studies (25). Therefore, the dosimetry simulations using real PET/CT imaging data of murine model might preclude the dose estimation errors aroused from the variations in individual organ anatomies and activity distributions. In this study, we performed voxel-based dosimetry of ^{18}F -FDG in normal mice from whole body PET/CT imaging to evaluate the feasibility and reliability of image-based preclinical dosimetry using GATE MC toolkit. More importantly, we applied the real CT and PET images of mice for GATE MC simulation instead of MOBY phantom. We also performed organ-based dosimetry using MIRD schema to compare with voxel-based absorbed dose obtained by GATE MC simulation.

1.2. Materials and Methods

1.2.1 Animal preparation

Thirteen 10–12 weeks old normal male C57BL/6 mice (body weight: 27.71 ± 4.25 g) were used in this study. All the procedures of this study were approved by the institutional Animal Care and Use Committee (IACUC) of Seoul National University Bundang Hospital (SNUBH), Seongnam, Korea (IACUC No. BA1708–229/072–01). The mice were kept at a room temperature of ca. 21 °C and ca. 55% humidity on a 12-h light/dark cycle, with food and water available ad libitum. The mice were fasted overnight for ^{18}F -FDG PET/CT imaging.

1.2.2 PET/CT Acquisition

The 90 min whole body dynamic PET acquisition was started with an IV injection of ^{18}F -FDG (15.22 ± 2.49 MBq) using NanoPET/CT system (Mediso Inc.,). An X-ray CT was performed after the PET scan to correct for gamma ray attenuation and to obtain anatomical information. Mice were maintained under 2% isoflurane anesthesia during the PET/CT scanning. Thirty-four dynamic frames ($4 \times 3\text{s}$, $6 \times 1\text{s}$, $7 \times 6\text{s}$, $8 \times 30\text{s}$, $1 \times 300\text{s}$ and $8 \times 600\text{s}$) were generated from the 90 min list mode data using iterative 3D ordered subset expectation maximization (OSEM) algorithm. Attenuation scattered and decay correction was applied during image reconstruction. A calibration factor was measured from uniform syringe phantoms (5 cc) filled with ^{18}F -FDG to correct for the activity concentration (Bq/ml) on reconstructed PET images of mice.

1.2.3 Organ mass estimation and image-based biodistribution

The volume of interests (VOIs) were manually drawn over the

major organs (brain, heart, lungs, liver, stomach, spleen, kidneys and urinary bladder) on CT and 90 minutes time integrated PET images (i.e., activity images representing the total duration of the study) as shown in figures 1.1 (a) and (b). The number of voxels in each organ were calculated and multiplied by the voxel volume and tissue density [(ICRP, 2002) (39)] to estimate the organ mass. The ^{18}F -FDG uptakes in the organs were estimated by applying VOIs over the organs on all reconstructed PET images as shown in figures 1.1 (c) to (h).

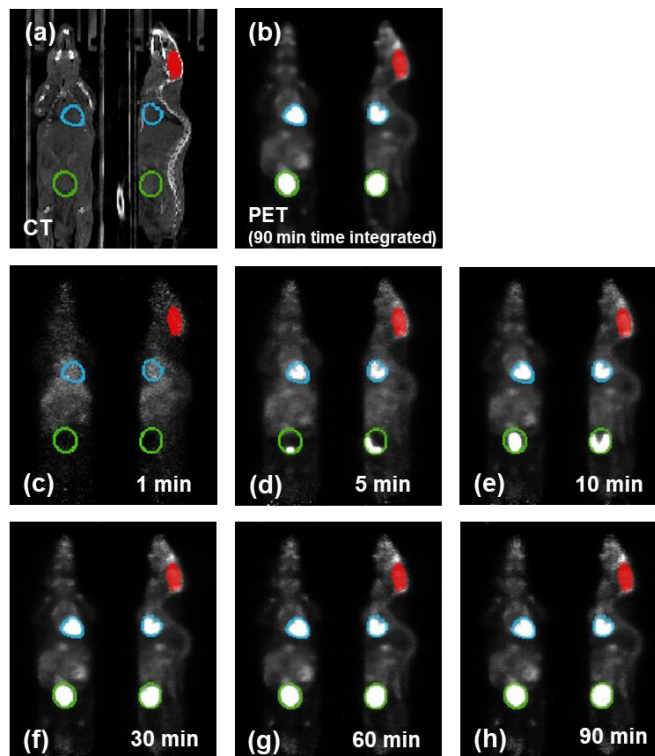


Figure. 1.1. VOIs drawn on brain, heart wall and bladder wall on CT images (a) and 90 minutes time integrated PET image (b). Figure shows the VOIs are superimposed on selected PET frames (c-h) at different time post injection. Coronal (left) and sagittal (right) views of CT and PET images are shown respectively in the figure.

The measured activity in the organs (MBq) was normalized to the total injected dose to obtain percentage-injected dose (%ID) and plotted as a function of time to generate time activity curves (TACs). The time-integrated activity (\bar{A}) in each organ was obtained by the trapezoidal sum of the area under curve (AUC) of TACs until ninety minutes and extrapolated to infinity using equation. (1.1). In equation (1.1), $A(t)$ is the activity of each organ at time t .

$$\bar{A} = \int_0^{\infty} A(t) dt = \int_0^{\infty} A_0 \exp\left(-\frac{\ln(2)}{T_{1/2}} t\right) dt \quad (1.1)$$

1.2.4 GATE MC simulation

GATE v. 7.0 was used for voxel-based absorbed dose calculation. GATE is based on the Geant4 toolkit (Geant4 v. 9.6.3), a well-established code for radiation transport. The real CT and PET image of mice were used as voxelized phantom and voxelized source respectively as the inputs in GATE for dosimetry simulation. The ^{18}F ion source type of Geant4 v. 9.6.3 was used for the simulation. GATE's standard electromagnetic physics package, which includes photoelectric effect, Compton, bremsstrahlung and positron-electron annihilation, was used during all simulations. In-house computing cluster with a 60-core CPU and 80 GB of RAM was used for the simulation of each PET frame with the corresponding biodistribution. The simulation was conducted for 10% of each PET frame duration to reduce the simulation time and extensive computational cost. However, the statistical uncertainties were kept below 2% at the voxel level.

1.2.5 Voxel-based dosimetry method

The steps followed for absorbed dose estimation using GATE MC simulation have been illustrated in figure 1.2. By using DoseActor mechanism of GATE, deposited energy [J] in each organ was extracted from all thirty-four Edep maps using same VOIs drawn earlier (mentioned in section 1.2.3). Subsequently, the absorbed dose in the organs was calculated and normalized to injected dose of ^{18}F -FDG in each mouse and presented as mGy/MBq. Moreover, the dose rates (Gy/sec) in the organs were measured and plotted against the function of time until ninety minutes and extrapolated to infinity to calculate the total absorbed dose in each organ.

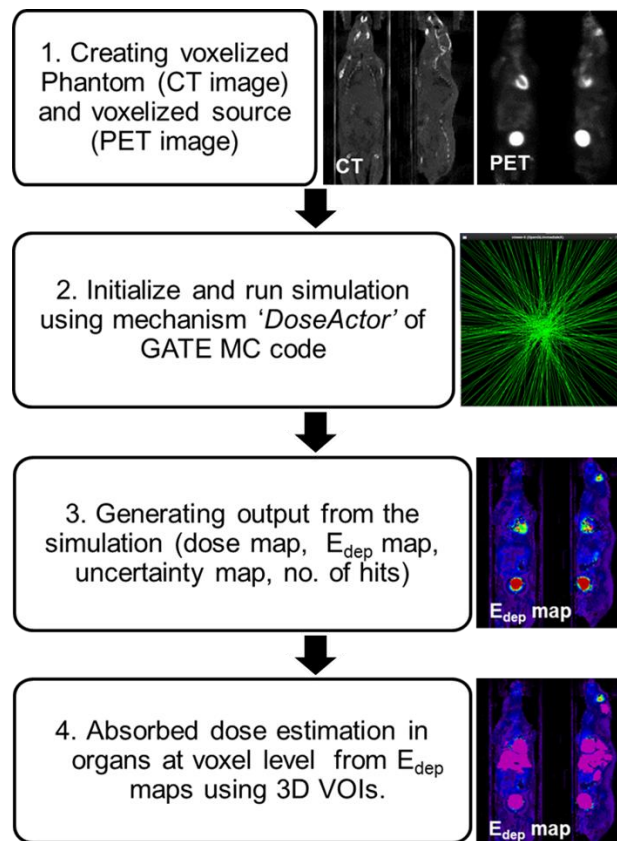


Figure 1.2. GATE MC simulation study for voxel-based absorbed dose estimation.

1.2.6 Organ-based dosimetry method

We conducted organ-based dosimetry based on the MIRD schema (40) using the same PET/CT imaging data for the comparison with voxel-based dosimetry. The mean absorbed dose (D) in the target organ (r_t) was calculated using the time-integrated activity (\tilde{A}) in the source organ (r_s) and S-value ($S(r_t \leftarrow r_s)$) given by the equation (1.2). Organ mass correction was performed while using S-values in MIRD formalism. The self and crossed absorbed S-values for the source-target organ pair were used from the published data by Xie et al. (41) to calculate self and cross-absorbed dose in each organ.

$$D(r_t \leftarrow r_s) = \tilde{A} \times S(r_t \leftarrow r_s) \quad (1.2)$$

1.3. Results

1.3.1. PET Image-based biodistribution

The TACs of eight organs are shown in the figure 1.3. The uptake of ^{18}F -FDG was the highest in liver followed by heart, lungs and brain. Kidneys were the main excretory organs for ^{18}F -FDG and hence the activity in the bladder was increased rapidly with the time, which was measured to be more than 25% of the total injected dose. The activity uptake in the other organs were minimal ($<2\%$).

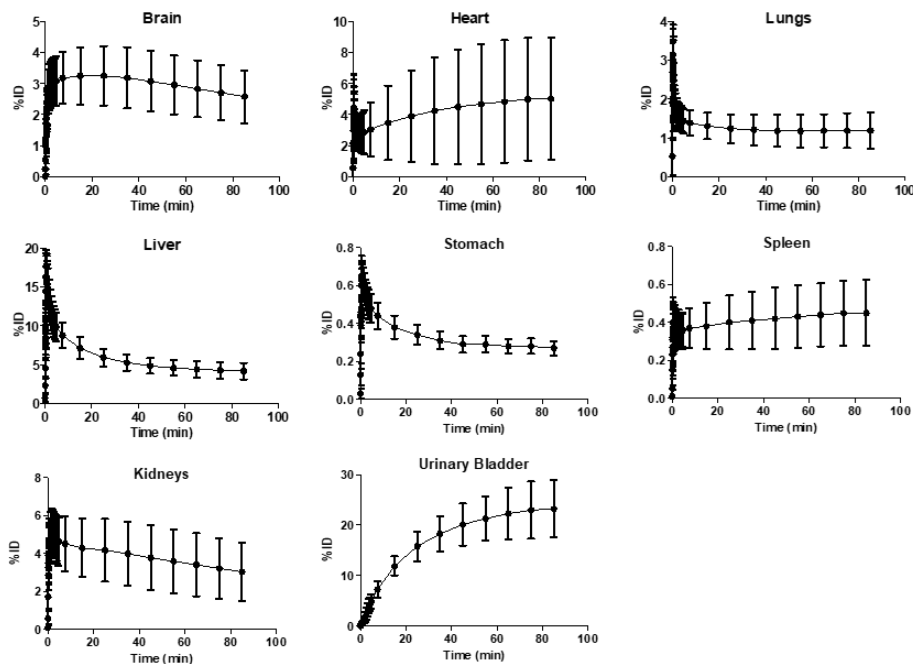


Figure 1.3. Percentage injected dose (%ID, mean \pm SD) versus time of the eight organs (corrected for radiation decay). SD, standard deviation.

1.3.2. Energy deposition and dose rate

The energy deposited in the organs as shown in the Edep map was

observed to be similar with the ^{18}F -FDG accumulation in the respective organs on PET images [Figure 1.4 (b)]. The 3D dose-rate vs. time graphs of eight organs are shown in figure 1.5.

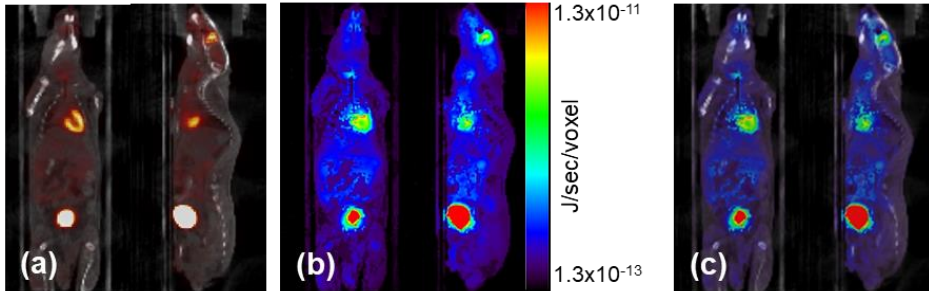


Figure 1.4. PET/CT fused image (a), Edep map (b) and the Edep map overlaid on CT image (c). The Edep map shows the energy deposited was higher for bladder wall, heart wall, kidneys and brain compared to other organs. Coronal (left) and sagittal (right) views of the images are shown respectively in the figure.

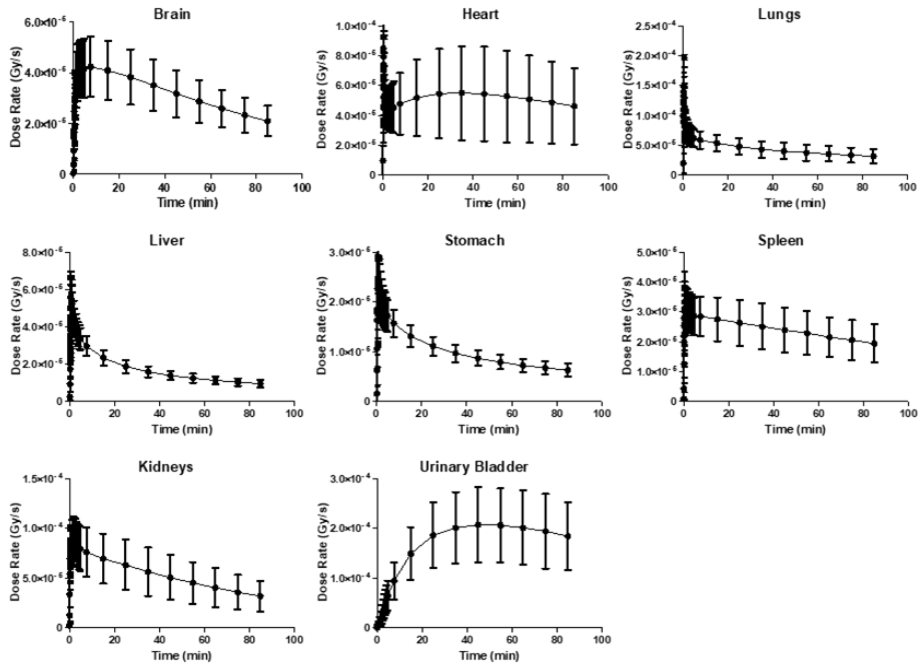


Figure 1.5. Dose-rate (mean \pm SD) versus time graph for the eight organs (uncorrected for radiation decay). SD, standard deviation.

1.3.3. Voxel-based absorbed dose

The voxel-based absorbed dose (mGy/MBq) in the major organs estimated by GATE MC simulation are presented in Table 1.1. Urinary bladder wall received the highest absorbed dose, which was followed by the heart wall, kidneys, lungs and brain. The reported absorbed dose values estimated in any organ by GATE MC are the sum of self and cross-absorbed dose. The absorbed doses in the same organs were different for different mouse because of the variations in organ anatomy and radiotracer biodistributions.

1.3.4. Organ-based absorbed dose

We calculated the self, cross and total organ absorbed doses using MIRD schema and the values (mGy/MBq) and are presented in the Table 1.2. We would like to point out that the S-values estimated by Xie et al. (41) were based on MOBY phantom. We applied mass correction for S-values in our real mouse studies for organ-based absorbed dose calculation.

Table 1.1. Voxel-based absorbed dose estimated in major organs (mean \pm SD) from ^{18}F -FDG using GATE MC.

Organs	Voxel-based absorbed dose (mGy/MBq)
Brain	24.29 \pm 7.28
Heart wall	48.14 \pm 30.96
Liver	11.94 \pm 2.73
Lungs	36.27 \pm 18.10
Stomach wall	7.29 \pm 0.77
Spleen	20.56 \pm 6.25
Kidneys	39.35 \pm 15.26
Bladder wall	174.76 \pm 61.29

Table 1.2. Organ-based absorbed dose (self, cross and total) estimated in major organs (mean \pm SD) from ^{18}F -FDG using MIRD schema normalized per MBq administered activity.

Organs	Organ-based absorbed dose (mGy/MBq)		
	Self-absorbed dose	Cross-absorbed dose	Total absorbed dose
Brain	22.39 \pm 6.98	1.52 \pm 0.52	23.91 \pm 7.04
Heart wall	35.32 \pm 29.44	6.33 \pm 1.83	41.65 \pm 31.05
Liver	10.00 \pm 2.16	4.44 \pm 1.97	14.44 \pm 3.22
Lungs	32.39 \pm 10.91	5.45 \pm 1.85	37.84 \pm 12.33
Stomach wall	5.22 \pm 0.62	3.29 \pm 0.70	8.51 \pm 0.93
Spleen	17.15 \pm 5.52	3.64 \pm 0.75	20.79 \pm 5.44
Kidneys	36.13 \pm 15.97	3.22 \pm 0.63	39.35 \pm 15.70
Bladder wall	158.47 \pm 57.12	9.49 \pm 6.06	167.96 \pm 58.71

1.3.5. Voxel-based vs. organ-based absorbed dose

The percentage difference in absorbed doses between voxel-based GATE method and organ-based MIRD schema were 1.36%, 12.34%, -22.37%, -11.21%, -16.85%, -2.87%, -4.29% and 3.71% for brain, heart wall, liver, lungs, stomach wall, spleen, kidneys and bladder wall respectively (Figure 1.6). The overall average difference in absorbed dose between these two dosimetry methods was -5.02%.

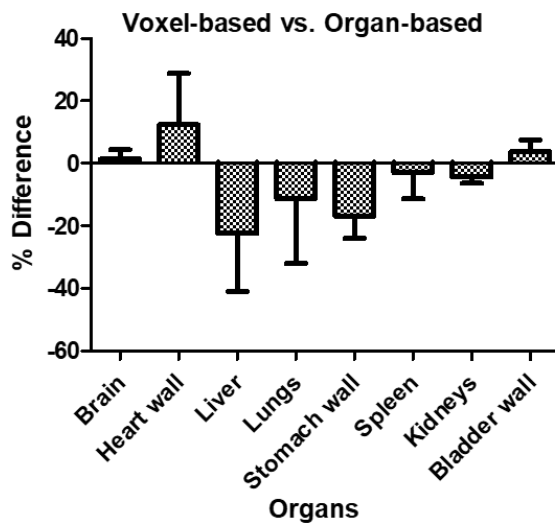


Figure 1.6. Percentage difference (mean \pm SD) between voxel-based absorbed dose estimated by GATE MC simulation and organ-based absorbed dose estimated by MIRD schema.

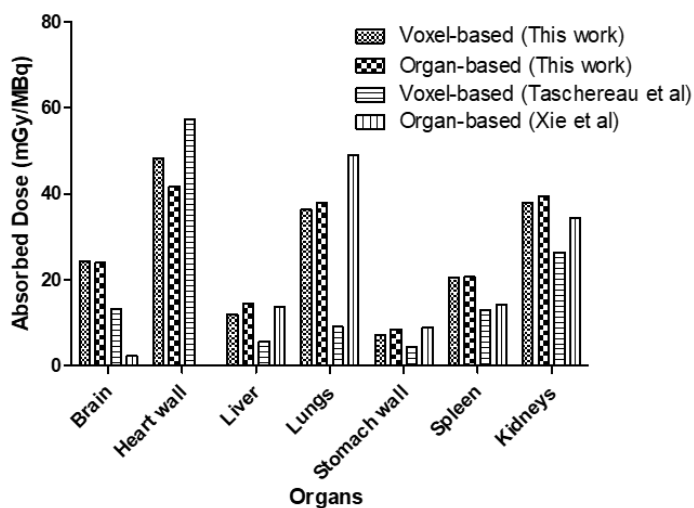


Fig. 1.7. Comparison of voxel-based and organ-based absorbed dose calculated from ^{18}F -FDG in selected organs of mice between this study and those reported by Xie et al. (41) and Taschereau and Chatziioannou (36).

1.4. Discussion

In this study, we explored the feasibility of GATE MC simulation to compute the absorbed dose at voxel-level in normal mice using ^{18}F -FDG. The voxel-based absorbed doses estimated by GATE MC simulation were comparable with the whole-organ absorbed doses based on MIRD schema. The highest differences of -22% (2.50 mGy/MBq) in the liver and -17% in the stomach wall (1.21 mGy/MBq) were due to the S-values applied in organ-based dosimetry using MIRD schema. The difference in mass and variations in anatomical position of organs in MOBY phantom might also be the reason for such differences in absorbed dose.

Furthermore, we compared our voxel- and organ-based dosimetry results with the published results (Figure 1.7). Firstly, we compared our voxel-based absorbed dose results with those reported by Taschereau and Chatziioannou (36) where they obtained 3D dose maps using GATE MC simulation and MOBY phantoms. The differences between the voxel-based absorbed doses in our study and Taschereau and Chatziioannou were principally due to the difference in PET data analysis methods and the different ^{18}F -FDG biodistributions between the mice species used. The additional discrepancies could be due to the difference in real mice anatomy used in our study and MOBY phantoms used in their study. The organ-based absorbed doses obtained in our study were also compared with those obtained by Xie et al. (41). They performed organ-based absorbed dose calculation using published mouse biodistribution data and S-values derived from their own study. Overall, there was good agreement between the estimated absorbed dose values in our work and those reported by Xie et al.

MC simulation is regarded as to yield the more realistic dose distribution in the organs at the voxel-level with high accuracy because it considers the true activity distribution and tissue heterogeneity in the entire body. Moreover, we used real PET/CT imaging data for dosimetry simulation, which obviates the variations in organ anatomy and activity distribution to produce the individualized whole-body energy distribution for each mouse. Therefore, the voxel-based absorbed dose estimated in the organs of mice from ^{18}F -FDG PET in our study would be more accurate and thus, this method can be applied in TRT for personalized dosimetry.

Chapter 2. Performance Evaluation of NanoSPECT/CT Scanner for ^{177}Lu imaging

2.1. Background

Small-animal SPECT/CT is widely used nowadays in biomedical research due to the possibility of translation of results from preclinical laboratories to the human clinical setting (13). The SPECT image qualities are fundamentally dependent on collimator type as well as the reconstruction technique (42). There is a trade-off between high spatial resolution and low sensitivity when using small-animal SPECT with pinhole collimator (13, 43). Number of approaches have been proposed to solve this issue and consequently, researchers have designed SPECT camera with multipinhole collimators that increases the system sensitivity while maintaining good spatial resolution (43-46).

Lutetium-177 (^{177}Lu) has several advantages: (a) low-energy beta emissions (498 keV); (b) shows efficient cross fire effects; (c) favorable half-life (6.73 days) and (d) emits adequate energy of gamma photons [208.4 keV (11%), 112.90 keV (6.4%)]. SPECT plays a fundamental role in TRT using ^{177}Lu however, during personalized dosimetry; both pre- and post-therapy SPECT studies must be quantitatively accurate because the reliable assessment of tumor uptake and tumor-to-normal tissue ratios can only be performed using quantitatively accurate images (47, 48). Hence, it is very important to evaluate performance parameters of preclinical SPECT systems for therapeutic radioisotopes before conducting pre- and post-therapy SPECT imaging or dosimetry studies.

In this chapter, we performed series of point source imaging and uniform phantom studies using ^{177}Lu and $^{99\text{m}}\text{Tc}$ sources to evaluate the quantitative accuracy and performance parameters of multipinhole mouse aperture of NanoSPECT/CT system. We measured recovery coefficient, uniformity, reconstructed spatial resolution and system sensitivity using both ^{177}Lu and $^{99\text{m}}\text{Tc}$. In addition, we measured calibration factor of mouse aperture of NanoSPECT/CT system for ^{177}Lu . We also compared the spatial resolution measured with and without adding uniform background to the point source data before image reconstruction.

2.2. Materials and Methods

2.2.1. NanoSPECT/CT system

The NanoSPECT/CT (Bioscan Inc.,) is a four-headed multipinhole small-animal SPECT imaging system. NanoSPECT/CT comes with series of dedicated multipinhole aperture suitable for imaging both mouse and rat using different diagnostic and therapeutic radioisotopes (49). In this study, we used mouse whole body standard aperture (NSP-108-M14-WB) for SPECT imaging using both ^{177}Lu and $^{99\text{m}}\text{Tc}$. The aperture has nine pinhole of 1.4 mm diameter. There are total 36 pinholes of four apertures mounted at four heads of the scanner. The axial and transaxial field of views (FOVs) for this mouse aperture are 14 mm and 30 mm respectively. The NanoSPECT/CT system has detector size of 350 mm \times 345 mm made up of NaI (Tl). It consists of 33 circular photo-multiplier tubes (PMTs) each of 2 inches in size. It also incorporates a cone beam CT for volumetric imaging through helical scanning.

2.2.2. Point source and uniform phantom acquisition

We used capillary tube having internal diameter of 1.1 mm to prepare point sources of ^{177}Lu and $^{99\text{m}}\text{Tc}$. The activities in the ^{177}Lu and $^{99\text{m}}\text{Tc}$ point sources were 1.78 MBq and 1.59 MBq respectively. Three different energy windows (20% width) were adopted for ^{177}Lu : 208.4 ± 20.84 keV, 112.9 ± 11.29 keV, and 56.30 ± 5.63 keV. For $^{99\text{m}}\text{Tc}$, 20% window was centered at 140 keV photopeak. First, the SPECT data was acquired with ^{177}Lu point source placed at the center of the axial and transaxial FOVs and repeated at every 2 mm from the center. Point source projection data were acquired at total 5 positions

(-4, -2, center, +2 and +4 mm) in axial and 9 positions (-8, -6, -4, -2, center, +2, +4, +6 and +8 mm) in transaxial FOVs as shown in figure 2.1. The whole procedure was repeated with ^{99m}Tc point source. The total scan duration for each point source acquisition was 10 min (10 projections with 60 sec/projection).

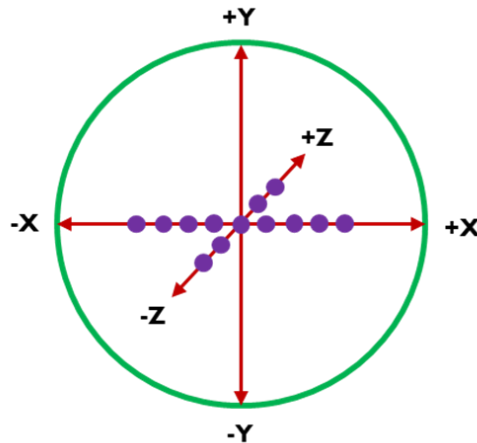


Figure 2.1. SPECT point source projections were acquired at center of axial and transaxial FOV and repeated at every 2 mm from the center. Axial FOV: 14 mm; Transaxial FOV: 30 mm.

Uniform phantoms were prepared using 20 ml disposable plastic syringes. The axial length and internal diameter of uniform phantom were 70 mm and 20 mm respectively. Two uniform phantoms, one containing ^{177}Lu and another containing ^{99m}Tc were prepared using the activity concentrations of 7.02×10^5 Bq/ml and 7.22×10^5 Bq/ml respectively. The volume of each phantom was 20 ml. We performed uniform phantom acquisitions using ^{177}Lu and ^{99m}Tc for: a) uniformity measurement and b) for background adding in the projection data of point sources. For uniformity measurement, large axial FOV (70 mm) was selected and the SPECT data were acquired for 44.92 min (35

projections with 77 sec/projection) for each radionuclide. The energy windows and photopeaks for the both radioisotopes used were same as applied for point source imaging.

2.2.3. Adding uniform background to point source data

It has been observed that if a point source image is reconstructed without any background, the reconstruction algorithms can enhance the apparent spatial resolution theoretically and it is not considered as reliable data (50). Hence, we added non-zero background to the point source data before reconstruction to mimic the real in vivo imaging conditions (51).

We acquired SPECT projection data of uniform phantoms with axial FOV of 14 mm for 2 hours (10 projections with 12 min/projection) to acquire enough counts. The uniform phantom projection was added to the projection data of point sources to create the uniform background in the reconstructed point source images. The uniform background data was added in such a way that the ratio of reconstructed point peak intensity to the mean background intensity was 10:1. The recovery coefficient, reconstructed SPECT uniformity in terms of percentage standard deviation (%SD) were measured from the uniform background added point source images.

2.2.4. Image reconstruction

SPECT point source and uniform phantom images were reconstructed by iterative image reconstruction method using HiSPECT NG software (Scivis GmbH, Germany). Iterative reconstruction for pinhole geometry has ability to correct for image degrading effects and provide better quantitative accuracy than

analytical reconstruction methods (52, 53). The point source imaging data were reconstructed in a $120 \times 120 \times 68$ matrix with voxel size of $0.30 \text{ mm} \times 0.30 \text{ mm} \times 0.30 \text{ mm}$ (recommended voxel size for the mouse whole body standard aperture). The point source images (with and without adding uniform background) were reconstructed with increasing numbers of iterations from three to thirty and the Gaussian filter was kept at its minimum value for spatial resolution measurement. However, we applied Gaussian filter during the reconstruction of point source data for the measurement of recovery coefficient and uniformity.

The SPECT images of uniform phantom were reconstructed using matrix size of $80 \times 80 \times 204$ and voxel size of $0.45 \text{ mm} \times 0.45 \text{ mm} \times 0.45 \text{ mm}$. The image were reconstructed with increasing number of iterations for the uniformity measurement. We applied Gaussian filter during the image reconstruction of uniform phantoms. We use similar reconstruction parameters during the preclinical SPECT imaging of mouse.

2.2.5. System performance evaluation

2.2.5.1. Recovery coefficient and uniformity measurement

We measured recovery coefficient (RC) and reconstructed SPECT uniformity of uniform background added point source images (central point in radial direction) of ^{177}Lu and $^{99\text{m}}\text{Tc}$ using equation 2.1 and 2.2 respectively. The volume of interests (VOIs) were drawn over each points and background areas using MRlcro tool as shown in figure 2.2 and 2.3. A cubic VOI (3.38 mm^3) containing 125 voxels was drawn over the point source image. For background area, four cylindrical VOIs were drawn each with the diameter and height of 4.5 mm and 1.5

mm respectively. The total number of voxels in the four cylindrical VOIs was 3240. In equation 2.1, $C_{recon\ point}$ is the average counts in the VOIs of reconstructed point image, $C_{recon\ bkg}$ is the average counts of the background VOIs and $R_{point/bkg}$ is the ratio of peak intensity of point to the average intensity of the background (10:1). We plotted measured RC vs. %SD with increasing iteration numbers.

$$RC = \frac{\left(C_{recon\ point} / C_{recon\ bkg} \right)}{R_{point/bkg}} \times 100\% \quad (2.1)$$

$$\%SD = \frac{SD}{\text{mean voxel value}} \times 100\% \quad (2.2)$$

The %SDs were also measured from uniform phantom images of ^{177}Lu and ^{99m}Tc using different iteration numbers. The VOIs were drawn over the central portion of uniform phantom images for uniformity measurements as shown in figure 2.4 (a) and (b).

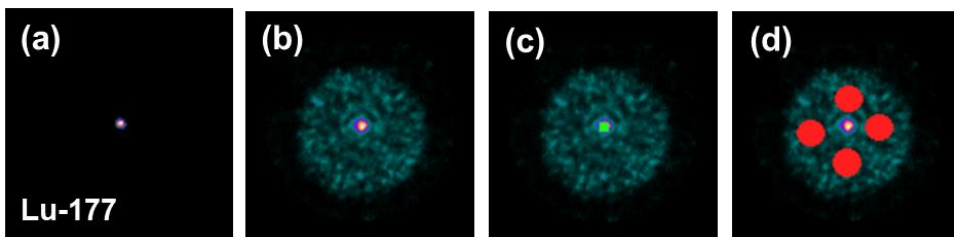


Figure 2.2. Reconstructed point source image of ^{177}Lu positioned at center of transaxial FOV. a) without background; b) after adding uniform background; c) VOIs drawn over background added point image; d) VOIs drawn over background regions.

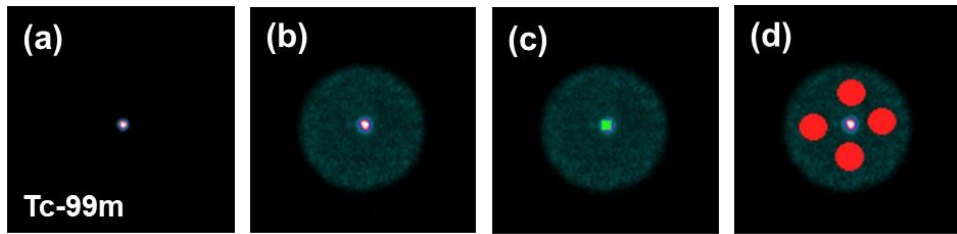


Figure 2.3. Reconstructed point source image of ^{99m}Tc positioned at center of transaxial FOV. a) without background; b) after adding uniform background; c) VOIs drawn over background added point image; d) VOIs drawn over background regions.

2.2.5.2. Spatial resolution measurement

The spatial resolutions of mouse aperture in the term of full width at half of maximum (FWHM) were measured from ^{177}Lu and ^{99m}Tc point sources at each points in axial, radial and tangential direction with and without adding uniform background. Firstly, we analyzed the relationship between the recovery coefficient and uniformity measured from background added point source image at increasing number of iterations to find the optimum iteration value. Finally, we applied that iteration value for the measurement of the spatial resolutions for both ^{177}Lu and ^{99m}Tc .

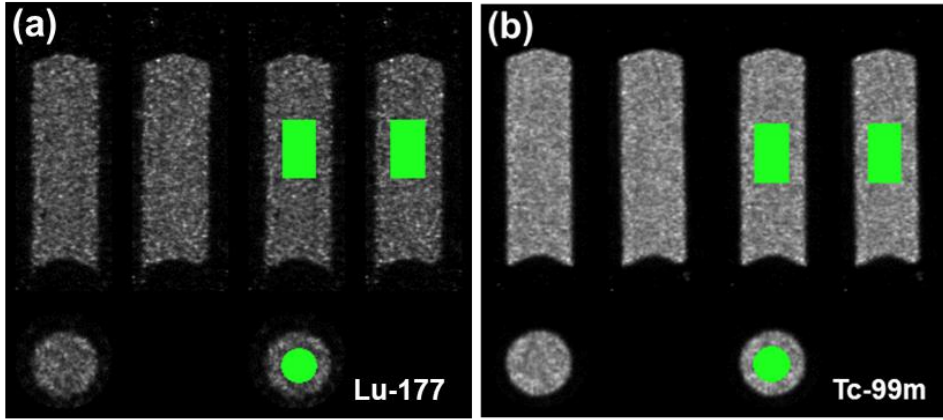


Figure 2.4. Reconstructed SPECT images of uniform phantoms containing ^{177}Lu (a) and $^{99\text{m}}\text{Tc}$ (b). VOIs were drawn over the central portion of the phantom images.

2.2.5.3. Sensitivity measurement

We measured the system sensitivity (cps/MBq) in axial and radial direction using the SPECT projection data of ^{177}Lu and $^{99\text{m}}\text{Tc}$ point sources acquired at different positions using equation 2.3. In this equation, N is the total counts measured, T_0 and T_s are the activity measurement and acquisition start time respectively, T_{half} is the half-life of radioisotope used, T_d is the scan duration of point source and A_0 is the initial activity in the point source.

$$\text{Sensitivity } (S) = \frac{N \times \exp^{\ln(2) \times (T_s - T_0) / T_{half}}}{T_d \times A_0} \quad (2.3)$$

2.2.5.4. Measurement of calibration factor

Calibration factor for ^{177}Lu was measured using reconstructed uniform phantom image for the conversion of counts to activity (Bq). VOIs were drawn over the uniform phantom image as shown in figure

2.4 (a). Mean VOI value (counts/voxel) were noted and the counts per milliliter (counts/ml) was measured which was further corrected for decay. Calibration factor (Bq/counts) was estimated by dividing the initial activity concentration (Bq/ml) in the phantom to the measured counts/ml.

2.3. Results

2.3.1. Recovery coefficient and uniformity

The recovery coefficients and percentage standard deviations were measured from uniform background added point source images of ^{177}Lu and $^{99\text{m}}\text{Tc}$ positioned at the center of transaxial FOV. Here, %SD uniformity is acquired from the background of point source imaging. We observed that more than 70% ^{177}Lu activity has been recovered at nine iterations with uniformity 30% SD (figure 2.5). The similar result was observed with $^{99\text{m}}\text{Tc}$ source where more than 72% $^{99\text{m}}\text{Tc}$ activity was recovered at nine iterations with less than 16% SD. When the iteration numbers were increased, recovery coefficient for both ^{177}Lu and $^{99\text{m}}\text{Tc}$ improved very slightly and reached to the plateau after 15 iterations as shown in figure. The recovery coefficients measured for ^{177}Lu and $^{99\text{m}}\text{Tc}$ were 79% and 80% respectively at 30 iterations. We found poor uniformity for ^{177}Lu compared to $^{99\text{m}}\text{Tc}$ however, the recovery coefficient for ^{177}Lu was comparable to $^{99\text{m}}\text{Tc}$.

The reconstructed SPECT uniformity of uniform phantoms were also measured with increasing iteration numbers. As shown in figure 2.6, we found the standard deviations of 25% and 13% for ^{177}Lu and $^{99\text{m}}\text{Tc}$ uniform phantom images respectively. Compared to $^{99\text{m}}\text{Tc}$, we observed poor uniformity for ^{177}Lu at nine iterations. However, the uniformity was acceptable when using six iterations. Therefore, we can conclude that six iterations might be adequate to be used during the image reconstruction of SPECT imaging of mouse. Although the uniformity improved, the recovery coefficient may decrease with lower iterations if we refer to the point source uniformity analysis (figure 2.5). The uniformity of ^{177}Lu imaging can be improved by

increasing the scan duration to acquire sufficient counts.

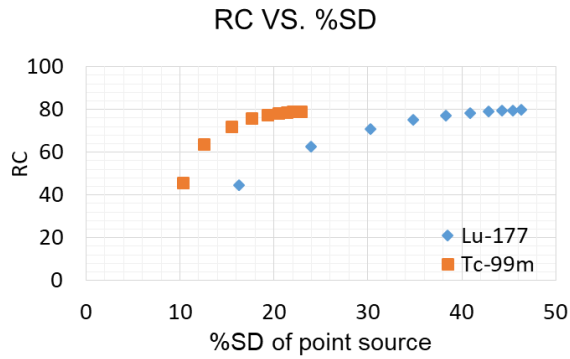


Figure 2.5. Scattered plot between recovery coefficients (RCs) and % SDs measured from reconstructed point source image with increasing number of iterations (3 to 30) for ^{177}Lu and $^{99\text{m}}\text{Tc}$. Iteration numbers are denoted by the shapes in the figure where first shape indicates three iterations; second shape indicates six and so on up to thirty iterations.

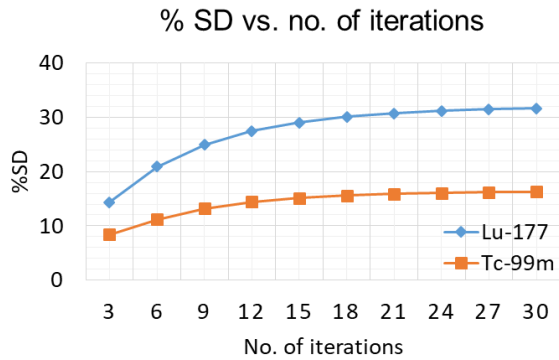


Figure 2.6. The relationship between %SDs of uniform phantom images and the number of iterations (3 to 30) for ^{177}Lu and $^{99\text{m}}\text{Tc}$.

2.3.2. Spatial resolution

We analyzed the relationship between recovery coefficient and uniformity of background added point sources with increasing number of iterations (figure 2.5) and found that the nine iterations would be more appropriate to measure the reconstructed spatial resolutions for both ^{177}Lu and $^{99\text{m}}\text{Tc}$.

The measured FWHM at center of FOV in axial, radial and tangential direction without adding background were 1.16 mm, 0.98 mm and 0.95 mm respectively for ^{177}Lu and 1.07 mm, 1.02 mm and 1.02 mm respectively for $^{99\text{m}}\text{Tc}$ when using nine iterations [figure 2.7 (a) and (b)]. We finally measured the FWHM values for all point source images at different positions (offsets from the center of FOVs) along axial, radial and tangential direction using the same iteration number as shown in figure 2.7 (a) and (b). We did not observe a large difference (<10%) in spatial resolutions measured at other positions in any direction for both radioisotopes.

The FWHM values were also obtained for both ^{177}Lu and $^{99\text{m}}\text{Tc}$ point sources after adding uniform background and compared the results with those without background. As shown in the figure 2.7 (a) and (b), we observed that the spatial resolution deteriorated when the uniform background was added to the point source images. The maximum increased FWHM values in axial, radial and tangential direction were 10%, 34% and 34% respectively for ^{177}Lu and 19%, 26% and 32 % for $^{99\text{m}}\text{Tc}$.

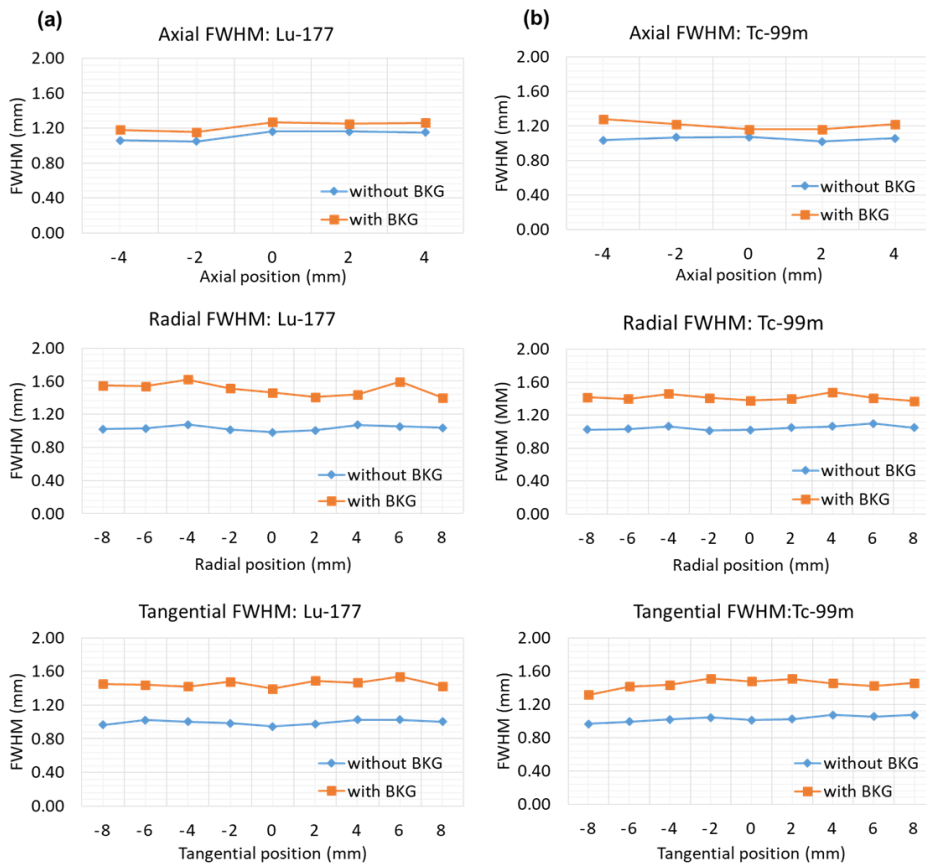


Figure 2.7. FWHM measured from ^{177}Lu (a) and $^{99\text{m}}\text{Tc}$ (b) point source images at center and other positions with and without adding uniform background in axial, radial and tangential directions. BKG, Background.

2.3.3. System sensitivity

The system sensitivity of multipinhole mouse aperture for both radioisotopes were the highest at the center of FOVs. The measured sensitivities at the center of axial and tranaxial FOVs were 389 and 401 cps/MBq respectively for ^{177}Lu and 1426 and 1489 cps/MBq respectively for $^{99\text{m}}\text{Tc}$. The decreasing trend in sensitivities for both radioisotopes were observed when the point sources moved from center towards the periphery in both axial and radial directions. The lowest sensitivities for ^{177}Lu (240 cps/MBq) and $^{99\text{m}}\text{Tc}$ (890 cps/MBq)

were noted at -4 mm offset from the center in axial FOV. In transaxial FOV, the lowest sensitivities measured for ^{177}Lu and $^{99\text{m}}\text{Tc}$ were 323 and 1082 cps/MBq respectively at -8 mm from the center. We found the sensitivity of ^{177}Lu was almost three times less when compared with that of $^{99\text{m}}\text{Tc}$.

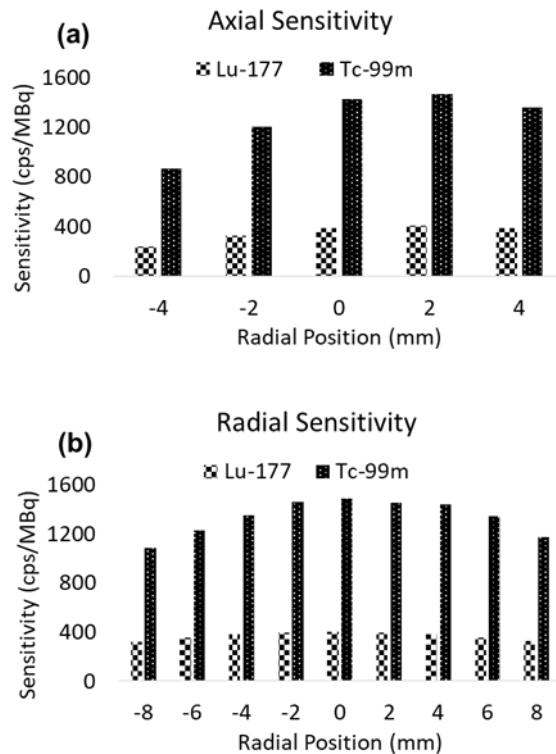


Figure 2.8. System sensitivities measured from ^{177}Lu and $^{99\text{m}}\text{Tc}$ point source projection data acquired at different positions in axial (a) and transaxial (b) FOVs.

2.3.4. Calibration factor

The reconstructed pixel intensity value of ^{177}Lu phantom images obtained from the NanoSPECT/CT system used in this study was given in counts. For quantitative analysis and for dosimetry purpose, the counts need to be converted into activity. The measured calibration factor from reconstructed uniform phantom image of ^{177}Lu was 10.85 Bq/counts. However, this measured calibration factor is not constant and should be measured each time before performing preclinical imaging. The NanoSPECT/CT system here was already calibrated for $^{99\text{m}}\text{Tc}$ source hence, the pixel intensity value for $^{99\text{m}}\text{Tc}$ phantom image was given in kBq. Consequently, there was no need to measure the calibration factor for $^{99\text{m}}\text{Tc}$.

2.4. Discussion

We evaluated the performance parameters of multipinhole mouse aperture of NanoSPECT/CT system for ^{177}Lu and $^{99\text{m}}\text{Tc}$ using point source imaging and uniform phantom studies. According to our knowledge, there is no such study performed earlier for ^{177}Lu however, very limited number of studies have been published to evaluate the quantitative accuracy of this system using $^{99\text{m}}\text{Tc}$. We found that the results obtained for $^{99\text{m}}\text{Tc}$ in our study were very similar to those published by various researchers (49, 54, 55). In this study, we used identical point sources and uniform phantoms as well as similar imaging conditions for both ^{177}Lu and $^{99\text{m}}\text{Tc}$ radioisotopes. Therefore, we believed that the results obtained for all the performance parameters (recovery coefficient, reconstructed SPECT uniformity, reconstructed spatial resolution and system sensitivity) evaluated in this study for ^{177}Lu radionuclide are reliable.

The performance parameters evaluated in this study play crucial role in the accuracy of activity quantification while performing pre- and post-therapy SPECT imaging of mouse for personalized dosimetry. Our study investigated the relationship between activity recovery and reconstructed image uniformity at different iteration numbers. The recovery coefficient of more than 70% was achieved for ^{177}Lu at optimum noise level when nine iterations were used. The spatial resolutions of ^{177}Lu with and without adding uniform background were comparable to that of $^{99\text{m}}\text{Tc}$ in all directions. System sensitivity for ^{177}Lu was almost three times less than that of $^{99\text{m}}\text{Tc}$ however; it is adequate to obtain quantitatively accurate SPECT images for personalized dosimetry.

Chapter 3. Voxel-based dosimetry of ^{177}Lu -labeled folate conjugates targeted SPECT/CT imaging of mice

3.1. Background

The selective concentration and prolonged retention of the radiopharmaceutical within the tumor is the basis for successful peptide-receptor radionuclide therapy (PRRT) (7). During radionuclide therapy, the toxicity and efficacy are of great concern and there is much less tolerance for inaccuracies in dosimetry hence, the voxel-based dosimetry is justified (15). Above all, SPECT/CT-based individualized dosimetry may be crucial where the average absorbed dose to an organ does not provide the information required to predict the potential biologic effects (15, 56, 57).

Folate receptors (FRs) are highly expressed in many human malignancies such as ovarian, cervical, renal, lung and breast carcinomas but there are very limited expression of these receptors in normal organs and tissues (10, 16, 58). Folic acid conjugate of therapeutic radioisotope especially ^{177}Lu has been a valuable tool to implement novel and effective anticancer therapies (59, 60). However, the high kidney absorbed dose due to the presence of FRs in proximal tubule cells remained a hurdle during TRT of FR-positive cancers (17-19).

Folate-based radiopharmaceuticals with prolonged blood circulation and high tumor retention time could overcome the dissatisfying situation mentioned above (16). IONPs have a large

surface area that provide a large number of functional groups for cross-linking to tumor-targeting ligands such as monoclonal antibodies, peptides, or small molecules for diagnostic imaging or targeted therapy (21). In this study, IONPs based ^{177}Lu -labeled folate conjugate (^{177}Lu -IONPs-Folate) was synthesized to evaluate the tissue distribution and to perform voxel-based dosimetry using ^{177}Lu -IONPs-Folate targeted SPECT/CT imaging of normal mice. We also estimated voxel-based absorbed dose in mice using with ^{177}Lu -Folate and ^{177}Lu -IONPs to compare with those obtained from ^{177}Lu -IONPs-Folate. Additionally, we calculated organ-based absorbed dose due to these radiotracers using MIRD schema to compare with the voxel-based absorbed dose values.

3.2. Materials and Methods

3.2.1. Synthesis of ^{177}Lu -labeled folate conjugates

3.2.1.1. *General*

Magnetic iron oxide nanoparticles (IONPs, 5 nm) in nonpolar solvent (chloroform) were provided from School of Advanced Materials Engineering, Kookmin University. All other reagents and solvents were purchased from Sigma-Aldrich (MO, USA). The hydrodynamic diameter and size distribution of nanoparticles were analyzed by a dynamic light scattering (DLS) system, Zetasizer Nano ZS90 (Malvern Instruments Ltd, Worcestershire, UK) and JEM-1010 transmission electron microscope (TEM; JEOL, Tokyo, Japan). The $^{177}\text{LuCl}$ was purchased from ITG GmbH (Munich, Germany). Instant thin layer chromatography-silica gel (ITLC-SG) plates were obtained from Agilent Technologies, Inc. (CA, USA). In addition, radio-thin layer chromatography (radio TLC) was performed with a Bio-Scan AR-2000 System imaging scanner (Bioscan, WI, USA). Radioactivity was measured by a gamma scintillation counter (Packard Cobra II, GMI, NM, USA).

3.2.1.2. *Preparation of Clickable IONPs (IONPs-DBCO)*

Polysorbate 60 solutions at concentrations of 10% (v/v) in distilled water (10 ml) were added to DSPE-PEG (2000)-DBCO (dibenzocyclooctyne, 123 mg). The mixture was sonicated at 30°C for 30 min. To this micelle mixture (1.5 ml) in a 20 ml glass vial, 100 μl of IONPs solution (50 mg/ml in CHCl_3) was added and the mixture containing CHCl_3 was evaporated using a rotary evaporator. After sonication for 1 hour, the reaction mixture was centrifuged and purified at 40,000 rpm at 4°C for 2 hours using OptiPrep™ gradients.

After the purification, the gradients was removed by Amicon filter (Amicon Ultra-0.5, 100 kDa, Merck Millipore, 10000 rpm, 25°C, 2 min).

3.2.1.3. Preparation of ^{177}Lu -NOTA-DBCO or N_3

$^{177}\text{LuCl}_3$ (148 MBq, 4 μl) was added to 160 μl of 1 M sodium acetate buffer (pH 5.6), followed by the addition of NOTA-PEG₃-DBCO or NOTA-PEG₃-N₃ (1.34 μl , 2 nmol, 1 mg/ml in water). The mixture was incubated at 70°C for 10 min to give ^{177}Lu -NOTA-DBCO or N₃, which was used for labeling of Folate-N₃, IONPs-DBCO or IONPs-Folate-DBCO without further purification. The radiolabeling efficiency (LE = 99 %) was determined using ITLC after a radiolabeling procedure with 0.1 M citric acid as the mobile phase. The Rf of ^{177}Lu -NOTA-PEG₃-N₃ or ^{177}Lu -NOTA-ADIBO = 0.5-0.6; Rf of free radioisotope = 0.9-1.0.

3.2.1.4. Preparation of ^{177}Lu -Folate

To the 148 MBq of ^{177}Lu -NOTA-DBCO solution (165.34 μl , 2 nmol), 264 μl of Folate-N₃ (80 μg , 8 nmol) in sodium ascorbate solution (300 $\mu\text{g}/\text{ml}$) was added and vortexed at 38°C for 1 hour. The LE was 99% and the Rf of ^{177}Lu -Folate was 0.2-0.3.

3.2.1.5. Preparation of ^{177}Lu -IONPs

IONPs-DBCO (1.2 mg, 8 nmol) was added to the 148 MBq of ^{177}Lu -NOTA-N₃ solution (165.34 μl , 2 nmol) and vortexed at 38°C for 1 hour. The LE was 99% and the Rf of ^{177}Lu -IONPs was 0.2-0.3.

3.2.1.6. Preparation of ^{177}Lu -IONPs-Folate

To the IONPs-DBCO (1.2 mg, 8 nmol) solution in distilled water (10 ml), 33 μl of Folate-N₃ (10 μg , 1 nmol) in sodium ascorbate solution (300 $\mu\text{g}/\text{ml}$) was added and kept at 38°C for 15 min. The reaction

mixture was purified by desalting column (PD-10, GE Healthcare, WI, USA) and concentrated to 100 μ l by Amicon filter. IONPs-Folate-DBCO (100 μ l, 8 nmol) was added to the 148 MBq of ^{177}Lu -NOTA- N_3 solution (165.34 μ l, 2 nmol), and vortexed at 38°C for 1 hour. The LE was 99% and the Rf of ^{177}Lu -IONPs-Folate was 0.2-0.3.

3.2.2. Animal preparation

All the animal studies were approved by the institutional Animal Care and Use Committee (IACUC) of Seoul National University Hospital, Seoul, Korea. Specific pathogen-free 4-week old male BALB/c nude mice were used in this study. Normal rodent diet contains a high level of folate, and hence, the mice received a folate-free diet (A08112101, Research Diets Inc., New Brunswick, NJ, USA) for 3 weeks to reduce the serum folate level to a physiologic range. We prepared three groups (n=5, total mice=15) of normal mice for SPECT/CT imaging with three different radiopharmaceuticals (^{177}Lu -Folate, ^{177}Lu -IONPs and ^{177}Lu -IONPs-Folate).

3.2.3. ^{177}Lu -SPECT/CT Imaging

SPECT/CT imaging of mice was performed using four-headed NanoSPECT/CT (Bioscan Inc.,) scanner having multipinhole collimators. The detailed specifications of NanoSPECT/CT has been explained in chapter 2. We performed whole body SPECT/CT imaging of first group of mice via tail vein injection of ^{177}Lu -Folate (11.99 ± 1.57 MBq). Similarly, we acquired SPECT/CT imaging of second and third group of mice after injection of ^{177}Lu -IONPs (9.16 ± 1.21 MBq) and ^{177}Lu -IONPs-Folate (5.50 ± 0.10 MBq) respectively. We acquired six sequential SPECT (5-15 s per frame) followed by a CT scan

immediately after each radiotracer injection without moving mouse from imaging table. We further acquired a SPECT/CT of mice at 6 hour (30 s per frame), 24 hour (45 s per frame), 48 and 72 hours (60 s per frame) post injection of radiotracers. We could not acquire 72 hour SPECT/CT images of mice injected with ^{177}Lu -IONPs-Folate due to the technical error occurred in the NanoSPECT/CT scanner. SPECT scans were acquired with 40 projections (frames) at 18-degree angular step. The energy peaks of ^{177}Lu were set to $56.1 \text{ keV} \pm 10\%$, $112.9 \text{ keV} \pm 10\%$, and $208.4 \text{ keV} \pm 10\%$. The CT acquisition was performed to correct for gamma ray attenuation and to obtain anatomical information using 55 mA tube current and 145 kVp.

3.2.4. Image reconstruction

All the acquired SPECT data were iteratively reconstructed with six iterations using ordered subset expectation maximization reconstruction algorithm of HiSPECT NG software (Scivis GmbH, Germany). The reconstructed SPECT images have the matrix size of $80 \times 80 \times 222$ and voxel size of $0.45 \times 0.45 \times 0.45 \text{ mm}$. The CT projection data were reconstructed (real time) using cone-beam filtered back projection with a matrix size of $204 \times 204 \times 632$ and voxel size of $0.15 \times 0.15 \times 0.15 \text{ mm}$. The reconstructed SPECT and CT images were analyzed using InVivoScope software provided with NanoSPECT/CT system. The voxel intensity was given in counts, which was converted to activity (Bq) using the calibration factor of scanner for ^{177}Lu measured before mice imaging. The method for calibration factor measurement has been explained in chapter 2.

3.2.5. SPECT image-based biodistribution of radiotracers

The volume of interests (VOIs) were manually drawn over the major organs (brain, heart, lungs, liver, and kidneys) on CT images of mice acquired at different time points using MRIcro tool (figure 3.1). The number of voxels in each organ was estimated from VOIs and multiplied by the voxel volume and tissue density [(ICRP,2000) (39)] to estimate the organ mass.

The activity uptakes in the organs from ^{177}Lu -Folate, ^{177}Lu -IONPs and ^{177}Lu -IONPs-Folate were estimated by applying the VOIs (drawn on CT images) over the organs on respective SPECT images acquired at different time points. The activity (Bq) measured in the organs was normalized to the total injected dose of each radiotracers to obtain percentage injected dose (% ID). The SPECT image-based biodistribution were plotted as a function of time to generate time activity curves (TACs) of organs for three radiotracers. The time-integrated activity (\tilde{A}) in the organs due to these three radiotracers were also estimated using the trapezoidal sum of AUCs of TACs (Equation. 1.2).

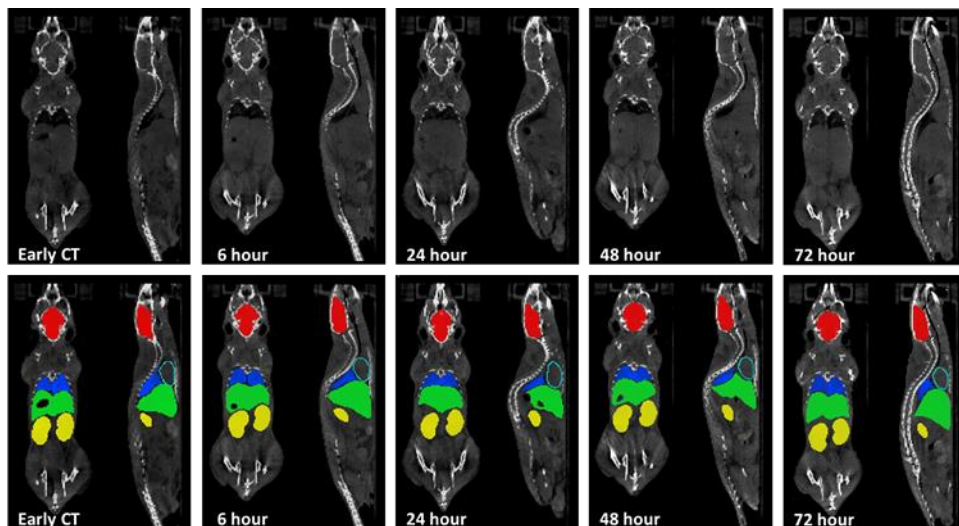


Figure 3.1. CT images acquired at different time points during

SPECT/CT acquisitions (upper row) of mice. VOIs were drawn over the organs (brain, heart, lungs, liver and kidneys on the CT images (lower row)).

3.2.6. GATE MC simulation set up

The GATE v.7.0 was used for the simulations to estimate voxel-based absorbed in the organs. The real CT and SPECT images of mice were modified to have the same voxel size ($0.45 \times 0.45 \times 0.45$ mm) and used as voxelized phantom and voxelized source respectively as the inputs in GATE for dosimetry simulation. The ^{177}Lu ion source type of Geant4 v. 9.6.3 was used for the simulation. A separate simulation for each SPECT image was run with corresponding biodistribution and scan duration. We run simulations for $1/100^{\text{th}}$ of the SPECT scan duration to reduce the simulation time and extensive computational cost. However, the statistical uncertainties were kept below 2% at the voxel level. The other simulation parameters used here were same as explained in the section 1.2.4 of chapter 2.

3.2.7. Voxel-based dosimetry method

GATE is provided with a mechanism, named *DoseActor*, which stores the absorbed dose in a given volume in a 3D matrix (61). The output of GATE simulation provides energy deposition (E_{dep}) map, dose distribution map, the number of hits and the local statistical uncertainty. By using *DoseActor* mechanism, deposited energy [J] in each organ was extracted from all ten E_{dep} maps of a mouse using VOIs previously drawn on CT images. The absorbed dose (Gy) in the organs was subsequently calculated from each E_{dep} map, which was further divided with respective simulation time to obtain dose rate (Gy/hr) in

the organs. The dose rate vs. time curves were plotted until 72 hours and extrapolated to infinity to measure the total voxel-based absorbed dose in the organs received by ^{177}Lu -Folate, ^{177}Lu -IONPs and ^{177}Lu -IONPs-Folate. The steps followed for absorbed dose estimation using GATE MC simulation has been illustrated in figure 1.2. The measured absorbed dose in the organs were normalized to the injected activity of radiotracers in each mouse study and presented as Gy/MBq.

3.2.8. Organ-based dosimetry method

We also calculated the organ-based absorbed dose (self-absorbed dose) received by organs due to ^{177}Lu -Folate, ^{177}Lu -IONPs and ^{177}Lu -IONPs-Folate using the MIRD schema. The mean absorbed dose (D) in the target organ (r_t) was calculated using the time-integrated activity (\tilde{A}) in the source organ (r_s) and self-absorbed S-value ($S(r_t \leftarrow r_s)$) given by the equation (1.2). The S-values for the source-target organ pair were used from the published data by Larsson et al. (62) to calculate self-absorbed dose in each organ. Organ mass correction was performed while using S-values in MIRD formalism. We compared the voxel-based absorbed dose in the organs received by all three radiotracers with the organ-based absorbed dose values obtained with MIRD schema.

3.3. Results

3.3.1. SPECT image-based biodistribution

In vivo SPECT/CT MIP images of normal mice obtained at different time points after the injection of ^{177}Lu -Folate, ^{177}Lu -IONPs and ^{177}Lu -IONPs-Folate are shown in figure 3.2(a), 3.2(b) and 3.2(c) respectively. The radioactivity of all three radiotracers were mainly accumulated in liver and kidneys immediately after the injection as shown in the early SPECT/CT images (figure 3.2). The TACs of brain, heart, lungs (left and right), liver and kidneys (left and right) obtained for all three radiotracers are shown in (figure 3.3). The highest accumulation of Lu-labeled conjugates were found in liver. The peak uptakes of ^{177}Lu -Folate, ^{177}Lu -IONPs and ^{177}Lu -IONPs-Folate in the liver were observed within 1 hour after injection which were $13.65 \pm 2.03\%$, $18.23 \pm 2.32\%$ and $16.07 \pm 1.40\%$ ID respectively [figure 3.3(a), 3.3(b) and 3.3(c)]. The peak uptakes of ^{177}Lu -Folate in the left and right kidneys were measured to be $5.04 \pm 0.81\%$ and $6.21 \pm 1.12\%$ ID respectively [figure 3.3(a)]; however, the peak uptakes of ^{177}Lu -IONPs-Folate were $3.45 \pm 1.04\%$ and $4.09 \pm 1.21\%$ ID respectively in left and right kidneys [figure 3.3(c)]. We observed that the renal uptake was less with the IONPs based ^{177}Lu -labeled folate conjugate compared to that without IONPs. The accumulation ^{177}Lu -IONPs in each kidney was less than 3%. The peak uptakes of all three radiotracers in brain, heart and lungs were less than 1.7% of total injected activities within one hour and gradually decreased with the time.

We found that the radioactivity in the liver due to all three ^{177}Lu radiotracers were decreased slowly. Even after 72 hours, the uptakes in liver were $6.39 \pm 0.68\%$ ID (^{177}Lu -Folate), $9.15 \pm 1.38\%$ ID (^{177}Lu -

IONPs) and $7.56 \pm 0.40\%$ ID (^{177}Lu -IONPs-Folate). The uptake in the left and right kidneys after 72 hours were $1.06 \pm 0.18\%$ and $1.36 \pm 0.17\%$ ID respectively for ^{177}Lu -Folate, $0.14 \pm 0.03\%$ and $0.20 \pm 0.02\%$ ID respectively for ^{177}Lu -IONPs and $0.34 \pm 0.04\%$ and $0.38 \pm 0.04\%$ ID respectively for ^{177}Lu -IONPs-Folate.

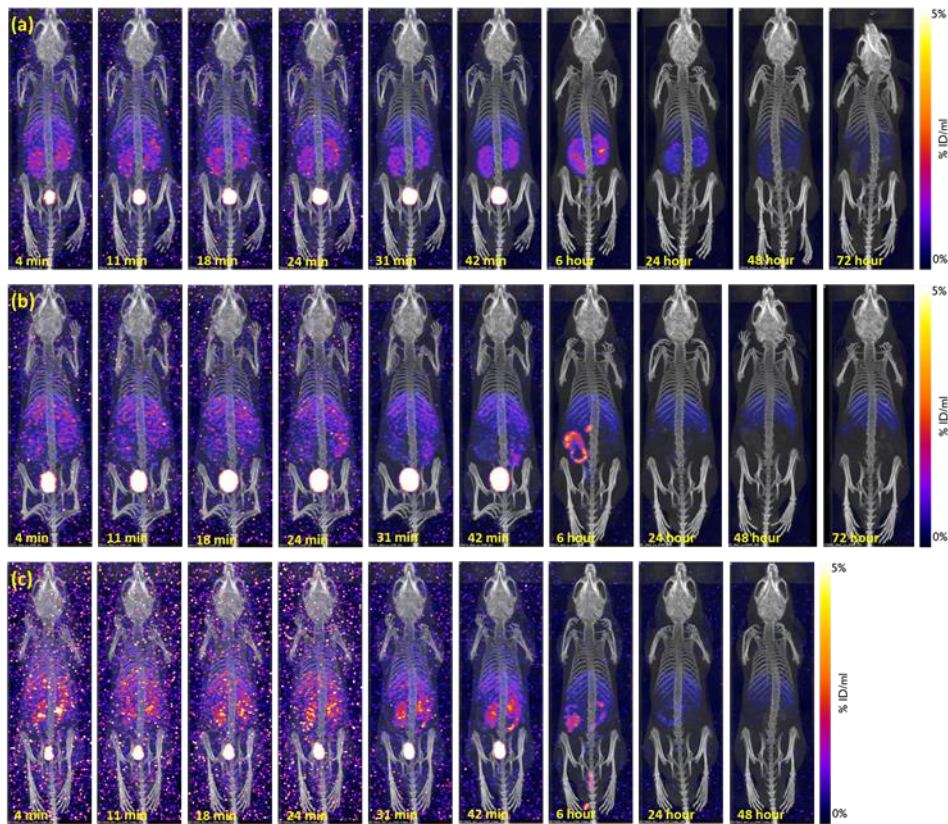


Figure 3.2. SPECT/CT MIP images of a mouse acquired at different time points after injection of ^{177}Lu -Folate (a), ^{177}Lu -IONPs (b) and ^{177}Lu -IONPs-Folate (c). For ^{177}Lu -IONPs-Folate, 72-hour image could not be acquired due to technical problem in the scanner.

3.3.2. Energy deposition and dose rate

The E_{dep} maps were obtained as the output of the simulation for each radiotracers and the 3D dose rate in the organs of mice was measured at different time points using the E_{dep} maps. The 3D dose

rates (Gy/hr) in organs were plotted with the function of time to generate dose rate curves for each radiotracers as shown in figure 3.4.

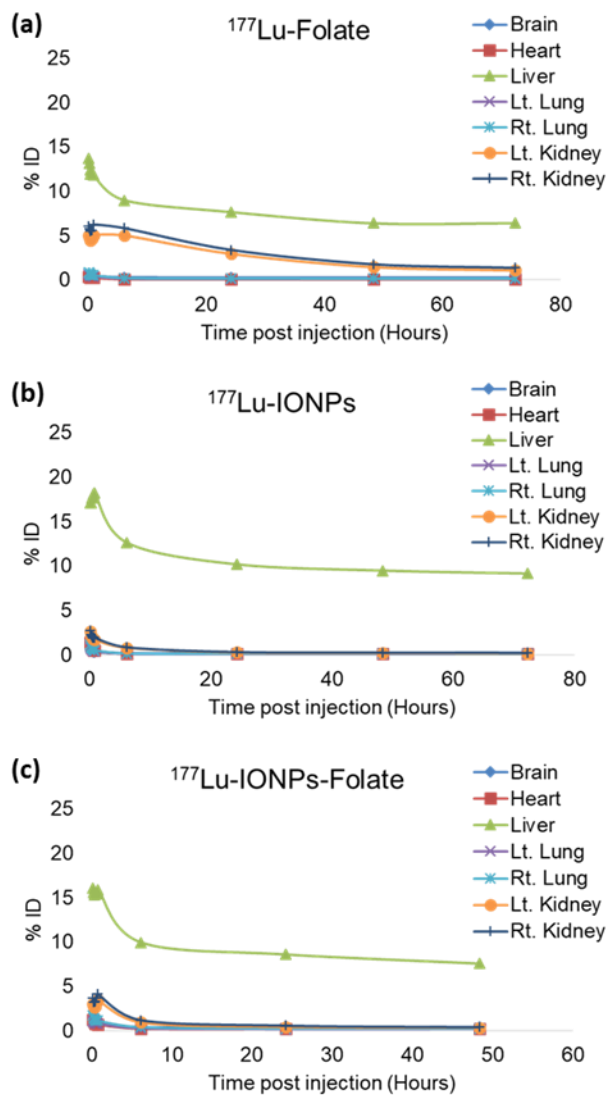


Figure 3.3. Percentage injected dose (%ID, mean) versus time graphs (TACs) of organs (corrected for radiation decay) obtained for $^{177}\text{Lu-Folate}$ (a), $^{177}\text{Lu-IONPs}$ (b) and $^{177}\text{Lu-IONPs-Folate}$ (c).

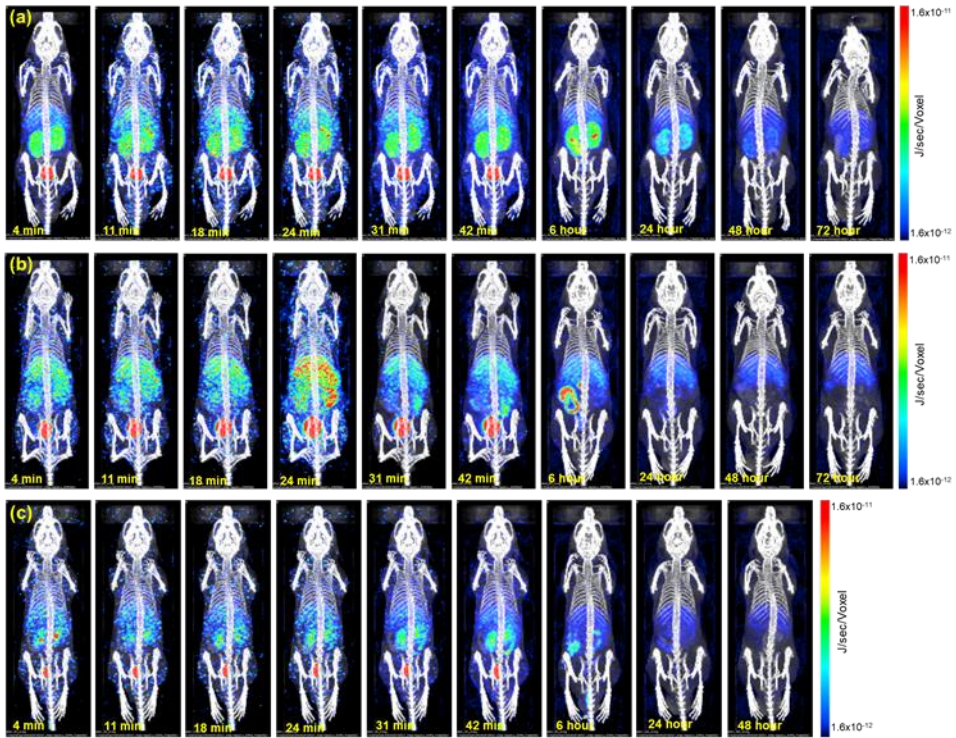


Figure 3.4. E_{dep} maps (obtained from GATE simulation of SPECT/CT imaging data) overlaid on CT (MIP images) images of mouse. ^{177}Lu -Folate (a), ^{177}Lu -IONPs (b) and ^{177}Lu -IONPs-Folate (c).

3.3.3. Voxel-based absorbed dose

The voxel-based absorbed dose (Gy/MBq) in brain, heart wall, lungs, liver and kidneys measured due to ^{177}Lu -Folate, ^{177}Lu -IONPs and ^{177}Lu -IONPs-Folate are presented in the table 3.1. The graph was plotted to compare the voxel-based absorbed dose received by the organs due to three radiotracers (figure 3.5). As shown in the figure, the absorbed dose was highest in the kidneys (2.20 ± 0.38 Gy/MBq) due to ^{177}Lu -Folate. However, ^{177}Lu -IONPs-Folate and ^{177}Lu -IONPs delivered renal absorbed dose of 1.01 ± 0.17 and 0.46 ± 0.04 Gy/MBq respectively. The absorbed dose in the liver was highest (1.06 ± 0.23 Gy/MBq) due to ^{177}Lu -IONPs compared to other radiotracers because of the effect of IONPs. The absorbed dose to the kidneys due to ^{177}Lu -

IONPs-Folate was 1.16 ± 0.51 Gy/MBq less than that received by ^{177}Lu -Folate. The renal absorbed dose was reduced significantly when IONPs based ^{177}Lu -labeled folate conjugate was used. The maximum difference in absorbed dose to other organs was 0.38 ± 0.33 Gy/MBq for lungs due to ^{177}Lu -IONPs-Folate.

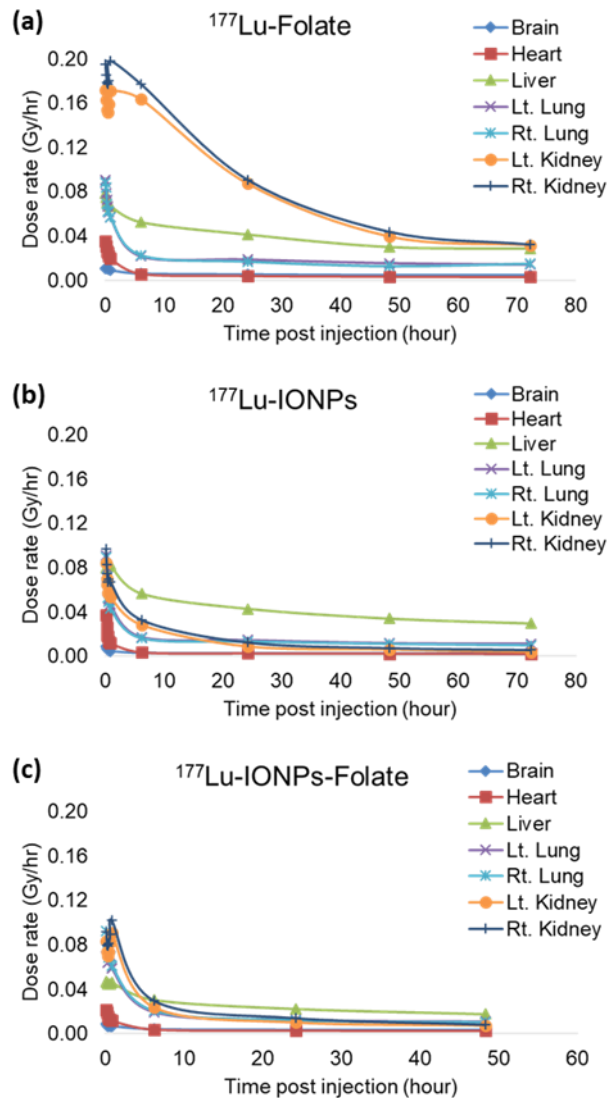


Figure 3.5. Dose-rate (mean) versus time graphs of organs (uncorrected for radiation decay) plotted for for ^{177}Lu -Folate (a), ^{177}Lu -IONPs (b) and ^{177}Lu -IONPs-Folate (c).

Table 3.1. Voxel-based absorbed dose (mean \pm SD) in major organs from ^{177}Lu -Folate, ^{177}Lu -IONPs and ^{177}Lu -IONPs-Folate.

Organs	Voxel-based absorbed dose (Gy/MBq)		
	^{177}Lu -Folate	^{177}Lu -IONPs	^{177}Lu -IONPs-Folate
Brain	0.13 \pm 0.02	0.09 \pm 0.01	0.18 \pm 0.02
Heart	0.09 \pm 0.01	0.07 \pm 0.01	0.14 \pm 0.01
Lungs	0.79 \pm 0.26	0.77 \pm 0.18	1.20 \pm 0.10
Liver	0.79 \pm 0.08	1.06 \pm 0.23	0.96 \pm 0.05
Kidneys	2.20 \pm 0.38	0.46 \pm 0.04	1.01 \pm 0.17

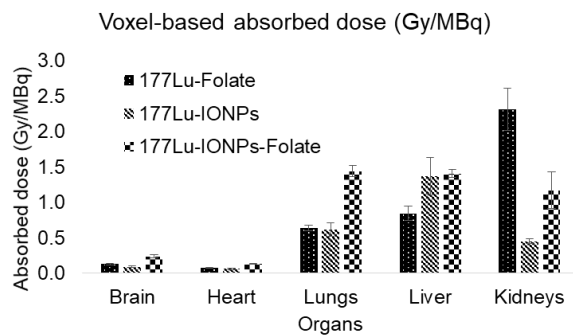


Figure 3.6. Comparison of voxel-based absorbed (mean \pm SD) in major organs from ^{177}Lu -Folate, ^{177}Lu -IONPs and ^{177}Lu -IONPs-Folate.

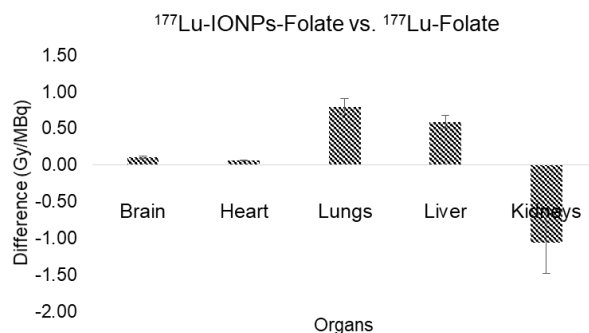


Figure 3.7. Difference in voxel-based absorbed dose (mean \pm SD) in organs between ^{177}Lu -IONPs-Folate and ^{177}Lu -Folate. The absorbed dose was significantly reduced with ^{177}Lu -IONPs-Folate.

3.3.4. Organ-based absorbed dose

We estimated organ-based self-absorbed dose (Gy/MBq) in the same organs due to all three radiotracers using MIRD schema and presented in Table 3.2. The self-absorbed dose estimated here are based on the radioactivity distributions in the organs of individual mouse however, the S-values used were estimated from MOBY phantom by Larsson et al.

Table 3.2. Organ-based absorbed (mean \pm SD) in major organs estimated by MIRD schema from ^{177}Lu -Folate, ^{177}Lu -IONPs and ^{177}Lu -IONPs-Folate.

Organs	Organ-based absorbed dose (Gy/MBq)		
	^{177}Lu -Folate	^{177}Lu -IONPs	^{177}Lu -IONPs-Folate
Brain	0.13 \pm 0.01	0.10 \pm 0.01	0.24 \pm 0.02
Heart	0.08 \pm 0.01	0.06 \pm 0.01	0.14 \pm 0.01
Lungs	0.64 \pm 0.04	0.62 \pm 0.04	1.40 \pm 0.13
Liver	0.84 \pm 0.10	1.27 \pm 0.21	1.29 \pm 0.05
Kidneys	2.32 \pm 0.30	0.49 \pm 0.05	1.22 \pm 0.21

We compared the measured voxel-based absorbed dose values obtained with GATE MC with the organ-based absorbed values (figure 3.7). We found the voxel-based absorbed dose values are comparable to organ-based self-absorbed dose in all organs due to ^{177}Lu -Folate and ^{177}Lu -IONPs. The organ-based self-absorbed dose in the organs were slightly higher than the voxel-based absorbed due to ^{177}Lu -IONPs-folate however; the highest difference is 0.26 Gy/MBq for liver (figure 3.8).

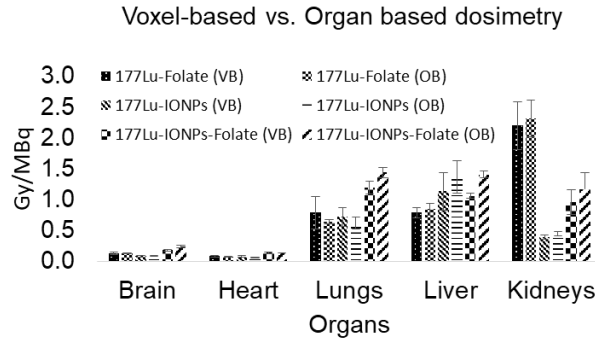


Figure 3.8. Comparison of voxel-based absorbed dose (mean \pm SD) estimated by GATE MC with organ-based self-absorbed dose (mean \pm SD) calculated with MIRD schema for ^{177}Lu -Folate, ^{177}Lu -IONPs and ^{177}Lu -IONPs-Folate. VB, voxel-based; OB, organ-based.

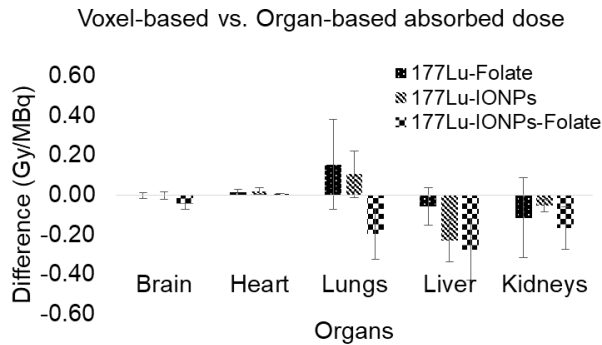


Figure 3.9. Difference between voxel-based absorbed dose (mean \pm SD) estimated by GATE MC and organ-based self-absorbed dose (mean \pm SD) calculated with MIRD schema for ^{177}Lu -Folate, ^{177}Lu -IONPs and ^{177}Lu -IONPs-Folate. Maximum difference was observed with ^{177}Lu -IONPs-Folate for liver.

3.4. Discussion

The pharmacokinetics of radiolabeled folic acid conjugates such as rapid clearance from blood circulation, high accumulation in kidneys and low retention in targeted tumor have been the major obstacles for the successful TRT of FR-positive cancers (10, 16). Because of these unsatisfactory kinetics of radiolabeled folates, the radiation dose absorbed to kidneys are very high compared to the tumors which necessitate the reduction in dosage of radiolabeled folate to be administered during targeted therapy. Therefore, the radiation energy absorbed in cancer cells from labeled therapeutic radionuclides cannot be sufficient for complete remission of the folate positive cancer.

In this study, we synthesized ^{177}Lu labeled folate radiopharmaceutical conjugated with IONPs (^{177}Lu -IONPs-Folate) with the aim of improving the overall tissue distribution and reducing the renal absorbed dose. We performed voxel-based dosimetry in normal mice using the ^{177}Lu -IONPs-Folate targeted SPECT/CT imaging. We also synthesized ^{177}Lu -Folate and ^{177}Lu -IONPs to perform dosimetry studies and compared the voxel-based absorbed dose received by these radiotracers in major organs. In addition, we calculated the organ-based self-absorbed dose using MIRD schema from these radiotracers and analyzed the differences in absorbed dose values between voxel-based and organ-based dosimetry methods.

The SPECT image-based biodistribution results showed the high and persistent accumulation of radioactivity (%ID) in the liver due to ^{177}Lu -IONPs and ^{177}Lu -IONPs-Folate compared to ^{177}Lu -Folate because of the effect of nanoparticles. Since the kidneys contain folate receptors, the renal uptake of ^{177}Lu -Folate was high and decreased very slowly compared to ^{177}Lu -IONPs and ^{177}Lu -IONPs-Folate. ^{177}Lu -

IONPs does not contain folate and hence very less uptake was seen in the kidneys. As we expected, the uptake of ^{177}Lu -IONPs-Folate in the kidneys was lower due to the presence of IONPs. Voxel-based absorbed dose measured was highest for kidneys followed by liver for all three ^{177}Lu radiopharmaceuticals. The voxel-based absorbed dose in kidneys delivered by ^{177}Lu -Folate was the highest however, the absorbed dose decreased significantly with ^{177}Lu -IONPs-Folate. Because of the presence IONPs, the kidneys uptake of ^{177}Lu -IONPs-Folate was low and cleared rapidly which decreased the absorbed dose to more than half when compared to ^{177}Lu -labeled folate conjugate without IONPs.

In a study performed by Muller et al. (16), they synthesized ^{177}Lu -cm09 (^{177}Lu labeled folic acid conjugate with albumin-binding entity) and estimated the self-absorbed dose in tumor xenografts (1.80 Gy/MBq) and kidneys (3.44 Gy/MBq) of FR-positive KB tumor bearing mice using MIRD schema. In our study, the voxel-based absorbed dose estimated in the kidneys of normal mice with ^{177}Lu -IONPs-Folate was 1.01 ± 0.17 Gy/MBq only. We found that the total absorbed dose in the kidneys measured at voxel-level was 5.53 ± 0.94 Gy due to the injection of 5.50 ± 0.10 MBq of ^{177}Lu -IONPs-Folate. The maximum tolerated dose to the kidneys is 25 to 30 Gy (63), which was almost 5 to 6 times higher than that we obtained with ^{177}Lu -IONPs-Folate. Therefore, we can administer nearly 30 MBq activity of ^{177}Lu -IONPs-Folate during the TRT of FR-positive tumor bearing mice to kill cancer cells more effectively without radiation nephropathy.

We expect that ^{177}Lu -IONPs-Folate will retain for longer period in tumor during the TRT of FR-positive cancers. In addition, the tumor to kidney absorbed dose ratio would increase and deliver high radiation dose to the tumor for successful targeted therapy.

We also compared the organ-based self-absorbed with voxel-based absorbed dose in the organs of each mouse for all three ^{177}Lu -radiotracers and found that the differences were not significant. The measured differences were mainly due to the S-values applied in organ-based dosimetry using MIRD schema. The S-values measured by Larsson et al. (62) were based on MOBY phantom. Therefore, the difference in mass and variations in anatomical position of organs in MOBY phantom and the real mice SPECT/CT imaging data used in our study might also be the reason for such differences in absorbed dose.

General Discussion and Conclusion

The normal tissue toxicity and efficacy are of great concern during radionuclide therapy and there is much less tolerance for inaccuracies in dosimetry, which justifies the role of the voxel-based dosimetry. MC simulation is regarded as to produce the more realistic dose distribution in the organs at the voxel-level with high precision since it considers tissue heterogeneity and the true activity distribution in the whole body.

In this thesis, we first evaluated the reliability and feasibility of GATE MC simulation using real PET/CT imaging data of normal mice to estimate whole-body absorbed dose at voxel-level. The voxel-based absorbed dose obtained was comparable to organ-based dose obtained with MIRD approach however; there was significant difference in the absorbed dose estimated in the liver and stomach wall. The difference were mainly due to the S-values applied in organ-based dosimetry using MIRD schema, which was based on MOBY phantom. Our voxel-based and organ-based absorbed dose results were also comparable with those published by other researchers (36, 41). We believed that GATE MC simulation toolkit could be applied for targeted radionuclide imaging and therapy for voxel-based absorbed dose estimation. Since the performance parameters of NanoSPECT/CT play crucial role in the accuracy of activity quantification while performing pre- and post-therapy SPECT imaging for personalized dosimetry, we performed series of phantom studies using ^{177}Lu and $^{99\text{m}}\text{Tc}$ sources to evaluate quantitative accuracy of the scanner for ^{177}Lu radioisotope. The results obtained for $^{99\text{m}}\text{Tc}$ in our study were very comparable to those published by various authors (49, 54, 55).

Hence, the performance parameters (recovery coefficient, reconstructed SPECT uniformity, reconstructed spatial resolution and system sensitivity) evaluated in this study for Lu-177 radionuclide would be reliable since the identical point sources, uniform phantoms as well as similar imaging conditions were applied for both ^{177}Lu and $^{99\text{m}}\text{Tc}$ radioisotopes. Finally, we performed voxel-based dosimetry in normal mice using the ^{177}Lu -labelled Folate conjugates targeted SPECT/CT imaging. We observed that the absorbed dose at voxel-level obtained with ^{177}Lu -IONPs-Folate was almost half compared to that obtained with ^{177}Lu -Folate because of the presence of iron-oxide nanoparticles. The total renal absorbed dose measured at voxel-level was 5.53 ± 0.94 Gy when 5.50 ± 0.10 MBq of ^{177}Lu -IONPs-Folate was injected. The maximum tolerated absorbed dose to the kidneys is 25 to 30 Gy (63). Hence, the administered activity of ^{177}Lu -IONPs-Folate can be increased up to 30 MBq during the TRT of FR-positive tumor bearing mice to kill cancer cells more effectively without radiation nephropathy.

In conclusion, we used real SPECT/CT imaging data of mice for MC simulation that obviates the variations in organ anatomy and activity distribution to produce the individualized whole-body energy distribution for each mouse. Hence, we believe that the voxel-based absorbed dose calculated in the organs of normal mice from ^{177}Lu -Folate, ^{177}Lu -IONPs and ^{177}Lu -IONPs-Folate in our study were more accurate and hence the same method can be applied during the TRT of FR-positive cancer for individualized dosimetry. Furthermore, during radionuclide therapy, the dose volume histograms (DVHs) can be obtained which provide information regarding the absorbed dose and inhomogeneous activity distribution within the target volume of tumor. This is particularly useful because it could be the starting point

for radiobiologic interpretation and modeling of the dose distribution for response assessment during cancer therapy.

Reference

- 1) Dash, A., Chakraborty, S., Pillai, M. R., & Knapp, F. F. (2015). Peptide receptor radionuclide therapy: an overview. *Cancer Biother. Radiopharm.*, 30(2), 47-71.
- 2) Flux, G., Bardies, M., Monsieurs, M., Savolainen, S., Strand, S. E., & Lassmann, M. (2006). The Impact of PET and SPECT on Dosimetry for Targeted Radionuclide Therapy. *Z. Med. Phys.*, 16(1), 47-59.
- 3) de Jong, M., Breeman, W. A., Bernard, B. F., Bakker, W. H., Schaar, M., van Gameren, A., et al. (2001). [¹⁷⁷Lu-DOTA0,Tyr3]octreotate for somatostatin receptor-targeted radionuclide therapy. *Int. J. Cancer.*, 92(5), 628-633.
- 4) de Jong, M., Valkema, R., Jamar, F., Kvols, L. K., Kwekkeboom, D. J., Breeman, W. A., et al. (2002). Somatostatin receptor-targeted radionuclide therapy of tumors: Preclinical and clinical findings. *Semin. Nucl. Med.*, 32(2), 133-140.
- 5) Pool, S. E., Krenning, E. P., Koning, G. A., van Eijck, C. H., Teunissen, J. J., Kam, B., et al. (2010). Preclinical and Clinical Studies of Peptide Receptor Radionuclide Therapy. *Semin. Nucl. Med.*, 40(3), 209-218.
- 6) Paganelli, G., Sansovini, M., Ambrosetti, A., Severi, S., Monti, M., Scarpi, E., et al. (2014). ¹⁷⁷Lu-Dota-octreotate radionuclide therapy of advanced gastrointestinal neuroendocrine tumors: results from a phase II study. *Eur. J. Nucl. Med. Mol. Imaging.*, 41(10), 1845-1851.
- 7) Ersahin, D., Doddamane, I., & Cheng, D. (2011). Targeted radionuclide therapy. *Cancers.*, 3(4), 3838-3855.
- 8) Giblin, M. F., Veerendra, B., & Smith, C. J. (2005). Radiometallation of Receptor-specific Peptides for Diagnosis and Treatment of Human Cancer. *In Vivo.*, 19(1), 9-29.
- 9) de Jong, M., Breeman, W. A., Kwekkeboom, D. J., Valkema, R., & Krenning, E. P. (2009). Tumor Imaging and Therapy Using Radiolabeled Somatostatin Analogues. *Acc. Chem. Res.*, 42(7),

873–880.

- 10) Müller, C., & Schibli, R. (2013). Prospects in folate receptor-targeted radionuclide therapy. *Front. Oncol.*, 3, 249.
- 11) Li, W. P., Lewis, J. S., Kim, J., Bugaj, J. E., Johnson, M. A., Erion, J. L., et al. (2002). DOTA-d-tyr1-octreotate: a somatostatin analogue for labeling with metal and halogen radionuclides for cancer imaging and therapy. *Bioconjug. Chem.*, 13(4), 721–728.
- 12) Willmann, J. K., van Bruggen, N., Dinkelborg, L. M., & Gambhir, S. S. (2008). Molecular imaging in drug development. *Nat. Rev. Drug Discov.*, 7(7), 591–607.
- 13) Franc, B. L., Acton, P. D., Mari, C., & Hasegawa, B. H. (2008). Small-animal SPECT and SPECT/CT: important tools for preclinical investigation. *J. Nucl. Med.*, 49(10), 1651–1663.
- 14) Hwang, A. B., Franc, B. L., Gullberg, G. T., & Hasegawa, B. H. (2008). Assessment of the sources of error affecting the quantitative accuracy of SPECT imaging in small animals. *Phys. Med. Biol.* 53(9), 2233–2252.
- 15) Dewaraja, Y. K., Frey, E. C., Sgouros, G., Brill, A. B., Roberson, P., Zanzonico, P. B., et al. (2012). MIRD Pamphlet No. 23: quantitative SPECT for patient-specific 3-dimensional dosimetry in internal radionuclide therapy. *J. Nucl. Med.*, 53(8), 1310–1325.
- 16) Müller, C., Struthers, H., Winiger, C., Zhernosekov, K., & Schibli, R. (2013). DOTA conjugate with an albumin-binding entity enables the first folic acid-targeted ^{177}Lu -radionuclide tumor therapy in mice. *J. Nucl. Med.*, 54(1), 124–131.
- 17) Birn, H., Spiegelstein, O., Christensen, E. I., & Finnell, R. H. (2005). Renal tubular reabsorption of folate mediated by folate binding protein 1. *J. Am. Soc. Nephrol.*, 16(3), 608–615.
- 18) Holm, J., Hansen, S. I., Høier-Madsen, M., & Bostad, L. (1992). A high-affinity folate binding protein in proximal tubule cells of human kidney. *Kidney Int.*, 41(1), 50–55.
- 19) Sandoval, R. M., Kennedy, M. D., Low, P. S., & Molitoris, B. A. (2004). Uptake and trafficking of fluorescent conjugates of folic acid in intact kidney determined using intravital two-photon microscopy. *Am. J. Physiol. Cell Physiol.*, 287(2), C517–C526.

- 20) Jarzyna, P. A., Skajaa, T., Gianella, A., Cormode, D. P., Samber, D. D., Dickson, S. D., et al. (2009). Iron oxide core oil-in-water emulsions as a multifunctional nanoparticle platform for tumor targeting and imaging. *Biomaterials.*, 30(36), 6947–6954.
- 21) Peng, X. H., Qian, X., Mao, H., Wang, A. Y., Chen, Z., Nie, S., & Shin, D. M. (2008). Targeted magnetic iron oxide nanoparticles for tumor imaging and therapy. *Int. J. Nanomedicine.*, 3(3), 311–321.
- 22) Yang, L., Peng, X. H., Wang, Y. A., Wang, X., Cao, Z., Ni, C., et al. (2009). Receptor-targeted nanoparticles for In vivo imaging of breast cancer. *Clin. Cancer Res.*, 15(14), 4722–4732.
- 23) Lee, D. S., Im, H. J., & Lee, Y. S. (2015). Radionanomedicine: Widened perspectives of molecular theragnosis. *Nanomedicine.*, 11(4), 795–810.
- 24) Kolbert, K. S., Watson, T., Matei, C., Xu, S., Koutcher, J. A., & Sgouros, G. (2003). Murine S factors for liver, spleen, and kidney. *J. Nucl. Med.*, 44(5), 784–791.
- 25) Theodora, K., Panagiotis, P., George, L., & George, C. K. (2016). A preclinical simulated dataset of S -values and investigation of the impact of rescaled organ masses using the MOBY phantom. *Phys. Med. Biol.*, 61(6), 2333–2355.
- 26) Hippeläinen, E., Tenhunen, M., & Sohlberg, A. (2015). Fast voxel-level dosimetry for ¹⁷⁷Lu labelled peptide treatments. *Phys. Med. Biol.*, 60(17), 6685–6700.
- 27) Stabin, M. G., Sparks, R. B., & Crowe, E. (2005). OLINDA/EXM: The Second-Generation Personal Computer Software for Internal Dose Assessment in Nuclear Medicine. *J. Nucl. Med.*, 46(6), 1023–1027.
- 28) Flynn, A. A., Green, A. J., Pedley, R. B., Boxer, G. M., Boden, R., & Begent, R. H. J. (2001). A mouse model for calculating the absorbed beta-particle dose from ¹³¹I- and ⁹⁰Y-labeled immunoconjugates, including a method for dealing with heterogeneity in kidney and tumor. *Radiat. Res.*, 156(1), 28–35.
- 29) Edmond, H. T., Fisher, D. R., Kuhn, J. A., Williams, L. E., Nourigat, C., Badger, C. C., et al. (1994). A mouse model for calculating cross-organ beta doses from yttrium-90-labeled

- immunoconjugates. *Cancer*, 73(S3), 951–957.
- 30) Muthuswamy, M. S., Roberson, P. L., & Buchsbaum, D. J. (1998). A mouse bone marrow dosimetry model. *J Nucl. Med.*, 39(7), 1243–1247.
- 31) Visvikis, D., Bardies, M., Chiavassa, S., Danford, C., Kirov, A., Lamare, F., et al. (2006). Use of the GATE Monte Carlo package for dosimetry applications. *Nucl. Instrum. Methods Phys. Res. A.*, 569(2), 335–340.
- 32) Jan, S., Santin, G., Strul, D., Staelens, S., Assié, K., Autret, D., et al. (2004). GATE: a simulation toolkit for PET and SPECT. *Phys. Med. Biol.*, 49(19), 4543–4561.
- 33) Agostinelli, S., Allison, J., Amako, K., Apostolakis, J., Araujo, H., Arce, P., et al. (2003). Geant4—a simulation toolkit. *Nucl. Instrum. Methods Phys. Res. A*, 506(3), 250–303.
- 34) Jan, S., Benoit, D., Becheva, E., Carlier, T., Cassol, F., Descourt, P., et al. (2011). GATE V6: a major enhancement of the GATE simulation platform enabling modelling of CT and radiotherapy. *Phys. Med. Biol.*, 56(4), 881–901.
- 35) Mauxion, T., Barbet, J., Suhard, J., Pouget, J. P., Poirot, M., & Bardies, M. (2013). Improved realism of hybrid mouse models may not be sufficient to generate reference dosimetric data. *Med. Phys.*, 40(5), 052501–n/a.
- 36) Taschereau, R., & Chatziioannou, A. F. (2007). Monte Carlo simulations of absorbed dose in a mouse phantom from 18-fluorine compounds. *Med. Phys.*, 34(3), 1026–1036.
- 37) Perrot, Y., Degoul, F., Auzeloux, P., Bonnet, M., Cachin, F., Chezal, J. M., et al. (2014). Internal dosimetry through GATE simulations of preclinical radiotherapy using a melanin-targeting ligand. *Phys. Med. Biol.*, 59(9), 2183–2198.
- 38) Segars, W. P., Tsui, B. M. W., Frey, E. C., Johnson, G. A., & Berr, S. S. (2004). Development of a 4-D digital mouse phantom for molecular imaging research. *Mol. Imaging Biol.*, 6(3), 149–159.
- 39) Valentin, J. (2002). Basic anatomical and physiological data for use in radiological protection: reference values: ICRP Publication 89. *Annals of the ICRP.*, 32(3), 1–277.

- 40) Bolch, W. E., Eckerman, K. F., Sgouros, G., & Thomas, S. R. (2009). MIRDPamphlet No. 21: A Generalized Schema for Radiopharmaceutical Dosimetry—Standardization of Nomenclature. *J. Nucl. Med.*, 50(3), 477–484.
- 41) Xie, T., & Zaidi, H. (2013). Monte Carlo-based evaluation of S-values in mouse models for positron-emitting radionuclides. *Phys. Med. Biol.*, 58(1), 169–182.
- 42) Lee, J. S., Kovalski, G., Sharir, & T., Lee, D. S. (2017). Advances in imaging instrumentation for nuclear cardiology. *J. Nucl. Cardiol.*, doi:10.1007/s12350-017-0979-8
- 43) Beekman, F. J., & Vastenhouw, B. (2004). Design and simulation of a high-resolution stationary SPECT system for small animals. *Phys. Med. Biol.*, 49(19), 4579–4592.
- 44) Schramm, N. U., Ebel, G., Engeland, U., Schurrat, T., Behe, M., & Behr, T. M. (2003). High-resolution SPECT using multipinhole collimation. *IEEE Trans. Nucl. Sci.*, 50(3), 315–320.
- 45) Schramm, N., Hoppin, J., Lackas, C., Forrer, F., Valkema, R., & de Jong, M. (2006). The NanoSPECT: A high-sensitivity multi-pinhole SPECT system with submillimeter (nanoliter) spatial resolution for imaging small rodents. *J. Nucl. Med.* 47(suppl 1), 233.
- 46) Difilippo, F. P. (2008). Design and performance of a multi-pinhole collimation device for small animal imaging with clinical SPECT and SPECT-CT scanners. *Phys. Med. Biol.*, 53(15), 4185–4201.
- 47) Zhang, L., Chen, H., Wang, L., Liu, T., Yeh, J., Lu, G., et al. (2010). Delivery of therapeutic radioisotopes using nanoparticle platforms: potential benefit in systemic radiation therapy. *Nanotechnol. Sci. Appl.*, 3(3), 159–170.
- 48) Shcherbinin, S., Piwowska-Bilska, H., Celler, A., & Birkenfeld, B. (2012). Quantitative SPECT/CT reconstruction for ^{177}Lu and $^{177}\text{Lu}/^{90}\text{Y}$ targeted radionuclide therapies. *Phys. Med. Biol.*, 57(18), 5733–5747.
- 49) Schramm, N., Hoppin, J., Lackas, C., Gershman, B., Norenberg, J., & de Jong, M. (2007). Improving resolution, sensitivity and applications for the NanoSPECT/CT: A high-performance SPECT/CT imager for small-animal research. *J. Nucl. Med.*,

- 48(suppl 2), 436.
- 50) Yang, Y., Tai, Y. C., Siegel, S., Newport, D. F., Bai, B., & Li, Q., et al. (2004). Optimization and performance evaluation of the microPET II scanner for in vivo small-animal imaging. *Phys. Med. Biol.*, 49(12), 2527-2545.
- 51) Gong, K., Cherry, S. R., & Qi, J. (2016). On the assessment of spatial resolution of PET systems with iterative image reconstruction. *Phys. Med. Biol.*, 61(5), N193-N202.
- 52) Bruyant, P. P. (2002). Analytic and Iterative Reconstruction Algorithms in SPECT. *J. Nucl. Med.*, 43(10), 1343-1358.
- 53) Israel-Jost, V., Choquet, P., Salmon, S., Blondet, C., Sonnendrucker, E., & Constantinesco, A. (2006). Pinhole SPECT imaging: compact projection/backprojection operator for efficient algebraic reconstruction. *IEEE Trans. Med. Imaging.*, 25(2), 158-167.
- 54) Harteveld, A. A., Meeuwis, A. P. W., Disselhorst, J. A., Slump, C. H., Oyen, W. J. G., Boerman, O. C., et al. (2011). Using the NEMA NU 4 PET Image Quality Phantom in Multipinhole Small-Animal SPECT. *J. Nucl. Med.*, 52(10), 1646-1653.
- 55) Cheng, D., Wang, Y., Liu, X., Pretorius, P. H., Liang, M., Rusckowski, M., et al. (2010). Comparison of ^{18}F PET and $^{99\text{m}}\text{Tc}$ SPECT Imaging in Phantoms and in Tumored Mice. *Bioconjug. Chem.*, 21(8), 1565-1570.
- 56) Dewaraja, Y. K., Wilderman, S. J., Koral, K. F., Kaminski, M. S., & Avram, A. M. (2009). Use of Integrated SPECT/CT Imaging for Tumor Dosimetry in I-131 Radioimmunotherapy: A Pilot Patient Study. *Cancer. Biother. Radiopharm.*, 24(4), 417-426.
- 57) Li, T., Ao, E. C. I., Lambert, B., Brans, B., Vandenberghe, S., & Mok, G. S. P. (2017). Quantitative Imaging for Targeted Radionuclide Therapy Dosimetry-Technical Review. *Theranostics.*, 7(18), 4551-4565.
- 58) Shen, H., Wang, L., Chen, W., Menard, K., Hong, Y., Tian, Y, et al. (2016). Tissue distribution and tumor uptake of folate receptor-targeted epothilone folate conjugate, BMS-753493, in CD2F1 mice after systemic administration. *Acta. Pharm. Sin. B.*, 6(5), 460-467.
- 59) Ke, C. Y., Mathias, C. J., & Green, M. A. (2004). Folate-receptor-

- targeted radionuclide imaging agents. *Adv. Drug. Deliv. Rev.*, 56(8), 1143–1160.
- 60) Segal, E. I., & Low, P. S. (2008). Tumor detection using folate receptor-targeted imaging agents. *Cancer Metast. Rev.*, 27(4), 655–664.
- 61) Sarrut, D., Bardiès, M., Boussion, N., Freud, N., Jan, S., Létang, J. M., et al. (2014). A review of the use and potential of the GATE Monte Carlo simulation code for radiation therapy and dosimetry applications. *Med. Phys.*, 41(6), 064301.
- 62) Larsson, E., Strand, S. E., Ljungberg, M., & Jönsson, B. A. (2007). Mouse S-Factors Based on Monte Carlo Simulations in the Anatomical Realistic Moby Phantom for Internal Dosimetry. *Cancer Biother. Radiopharm.*, 22(3), 438–442.
- 63) Vilchis-Juárez, A., Ferro-Flores, G., Santos-Cuevas, C., Morales-Avila, E., Ocampo-García, B., and Díaz-Nieto, L., et al. (2014). Molecular targeting radiotherapy with cyclo-RGDfK(C) peptides conjugated to ^{177}Lu -labeled gold nanoparticles in tumor-bearing mice. *J. Biomed. Nanotechnol.*, 10(3), 393–404.

초록

^{177}Lu 로 표지된 SPECT/CT용 엽산 복합체를 이용한 전임상 복셀 기반 선량 측정기법

펩타이드-수용체 방사성 핵종 치료 (PRRT)는 림프종, 아교모세포종, 신경 내분비 종양 및 전립선 암을 비롯한 다양한 암의 치료에 있어 그 중요성이 점점 커지고 있다. 표적 방사성 핵종 치료 (TRT)의 유효성은 주로 흡수 선량률과 종양 및 정상 조직에 전달되는 총 흡수 선량에 따라 결정된다. 따라서 치료의 유효성을 평가하기 위해서는 가능한 한 정확하게 흡수 선량을 측정 또는 계산해야 한다. MIRD 선량계산법을 따라 수행되는 장기 기반 선량 측정과 관련된 다양한 한계로 인해, 보다 정확한 흡수 선량을 평가하기 위해서는 복셀 기반 선량 측정법이 필요하다.

엽산 수용체 (FR)는 난소 암 및 자궁 경부암을 비롯한 다양한 종양과 관련된 표적 물질로 알려졌다. 따라서 진단 및 치료용 방사성 핵종들이 표지된 엽산 복합체들이 표적 이미징 및 치료를 위해 개발된 바 있다. 그러나 방사성 핵종들이 표지된 엽산 복합체를 이용한 치료는 신장에서의 높은 흡수 선량 때문에 임상 수준에서 아직 적용되지 못하고 있다. 이러한 문제점을 극복하기 위해 본 연구에서는 산화철 나노 입자 (IONP) 기반 방사성 엽산 복합체 (^{177}Lu -NOTA-IONP-Folate)를 조제하고, 정상 마우스의 SPECT / CT 영상을 기반으로 복셀 기반 선량 측정을 수행했다.

본 연구에서는 먼저 GATE 몬테카를로 시뮬레이션을 이용한 복셀 기반 선량 측정기법의 전임상 수준에서의 타당성과 신뢰성 평가를 위해 정상 마우스의 ^{18}F -fluorodeoxyglucose (^{18}F -FDG) PET / CT 영상을 적용하였다. 다음으로, ^{177}Lu 방사성 동위 원소에 대한 NanoSPECT / CT 스캐너의 시스템 성능과 정량성을 평가를 위하여 점 선원과 균일도

팬텀 스터디를 진행하였다. 측정된 성능 파라미터들은 전임상 SPECT / CT 이미징 및 선량 평가를 진행하기에 충분히 높은 정량적 정확도를 보였다. 마지막으로 정상 마우스의 ^{177}Lu -NOTA-IONP-Folate, ^{177}Lu -NOTA-IONP 및 ^{177}Lu -NOTA-Folate SPECT/CT 영상에 GATE 몬테카를로 시뮬레이션을 사용하여 복셀 수준의 흡수 선량을 추정했다. 철-산화물 나노 입자 기반의 ^{177}Lu 로 표지된 엽산 복합체 (^{177}Lu -NOTA-IONP-Folate)가 표적 방사성 핵종 치료에 사용되었을 때 신장의 흡수 선량이 유의미하게 감소한다는 것을 확인했다.

본 연구에서 적용한 복셀 기반 선량측정 기법은 실제 마우스 내의 선량 및 매질 분포를 사용하여 기존의 장기 기반 선량측정 기법보다 정확한 장기의 흡수 선량을 획득할 수 있다. 본 연구에서 평가된 복셀 기반 선량측정 기법은 방사성 핵종 치료와 같은 환자 기반 치료에서, 방사성 의약품의 최대 허용 투여량 및 타겟 장기에 전달되는 선량평가를 추정하는데 이용 가능하다.

주요어: SPECT/CT, 복셀 기반 선량 측정 기법, GATE 몬테카를로, ^{177}Lu , 엽산 수용체, IONP